Use Authorization

In presenting this thesis in partial fulfillment of the requirements for an advanced degree at Idaho State University, I agree that the Library shall make it freely available for inspection. I further state that permission for extensive copying of my thesis for scholarly purposes may be granted by the Dean of the Graduate School, Dean of my academic division, or by the University Librarian. It is understood that any copying or publication of this thesis for financial gain shall not be allowed without my written permission.

Signature _____

Date _____

Fuel Fracture Experimental Designs using Bison Fuel Performance Code for Out-of-Pile Separate-Effects Validation Experiments

by

Ju-Yuan Yeh

A thesis

submitted in partial fulfillment

of the requirements for the degree of

Master of Science in Nuclear Science and Engineering

Idaho State University

Fall 2018

COMMITTEE APPROVAL

To the Graduate Faculty:

The members of the committee appointed to examine the thesis of Ju-Yuan Yeh find it satisfactory and recommend that it be accepted.

Dr. Mary Lou Dunzik-Gougar,
Major Advisor

Dr. Benjamin Spencer,
Committee Member

Dr. Steve Chiu,
Graduate Faculty Representative

Acknowledgments

First, I would like to thank Dr. Dunzik-Gougar for giving me the opportunity to work on this Integrated Research Project (IRP), led by Dr. Ban at University of Pittsburgh (formally at Utah State University), and funded by the US Department Office of Nuclear Energy. I would also like to thank my mentor, Dr. Spencer in the Fuel Modeling and Simulation Department at Idaho National Laboratory. His guidance and patience was critical to my successes over the course of my research. I would also like to express my gratitude to all the PIs in this IRP project team, especially Dr. Besmann and Dr. Knight at University of South Carolina and Drs. McDeavitt, Ortega and Perez-Nunez at Texas A & M University for their collaborations in integrating experiment and computation for separate-effects fuel fracture research. Through this IRP project, I was very fortunate to have the opportunity to participate in one of the first TREAT irradiation experiments following restart. Finally I would like to thank my husband. Without his encouragement and support I would not have been able to finish this journey.

Table of Contents

List of Figures

List of Tables

Fuel Fracture Experimental Designs using Bison Fuel Performance Code for Out-of-Pile Separate-Effects Validation Experiments

Thesis Abstract–Idaho State University (2018)

First principles models of LWR (Light Water Reactor) UO_2 fuel cracking are being developed for the Bison fuel performance code. Model validation will be accomplished using data from out-of-pile experiments. The objective of work presented in this thesis is to guide design of experiments that will use different methods to create the temperature gradient near the pellet surface that is needed to induce cracking: (1) resistive heating and (2) quenching after bulk pre-heating. To guide (1), a temperature dependent electrical conductivity and resistive heating model was developed and coupled with the model for the thermal-mechanical aspects of fuel behavior. Key variables were the coolant heat transfer coefficient, initial temperature and amount of current. To guide (2), only the thermal-mechanical model was needed and key variables were the temperature difference in salt baths used for heating and cooling, thermal conductance of the gap between pellet and clad, and the coolant heat transfer coefficient. Though the out-pile-experiments will not reproduce volumetric heating like an LWR, the simulated cracking patterns for the experiments agree with those from LWRs.

Keywords: Fuel fracture, Bison, out-of-pile experiments, separate-effects, experiment design.

Chapter 1

Introduction

Ceramic uranium oxide fuel pellets are used in nuclear light water reactors (LWRs), which make up the majority (85%) of the commercial power reactors currently in use worldwide [Motta and Olander, 2017]. UO_2 was selected for its distinctive properties including high melting point (2850 °C), compatibility with water, excellent irradiation stability and ease of fabrication [Banerjee and Kutty, 2012]. Due to the low thermal conductivity of UO_2[1], these fuel pellets experience significant temperature gradients even during normal operation. This temperature gradient along with high thermal expansion coefficient[2], leads to nonuniform thermal expansion across the fuel cross section and generates high stress around the fuel pellet perimeter. The stress combined with low tensile strength (around 150 MPa) can result in initial cracking in the outside radius of the fuel pellet at a low power level ($5 \sim 7$ KW/m). This behavior has a significant influence on the overall thermal and mechanical behavior of the fuel system, and can potentially be a contributor to cladding failure due to pellet-cladding mechanical interaction (PCMI). Fracture also affects fuel redistribution during reactivity insertion and loss of coolant accidents. Many of these effects are incorporated into empirical models of fuel behavior under normal operating conditions. The limits of these correlations are they are only suitable in experimental data ranges. Realistic first principle physics-based

[1] Thermal conductivity k of UO_2 is 3.7 $W/m \cdot K$ verse 17 $W/m \cdot K$ for Zircaloy [Motta and Olander, 2017].

[2] Thermal expansion coefficient α (K^{-1}) of UO_2 is 1.45×10^{-5} and $5 \sim 10 \times 10^{-6}$ for Zircaloy [Motta and Olander, 2017].

modeling is necessary for better predictions under abnormal (accident) conditions.

1.1 Motivations for the Study

To model the fracturing process in LWR fuel, multiple computational cracking simulation techniques are included in the Bison fuel performance code. These techniques include smeared cracking, extended finite element method, peridynamics and phase field. As these fracture models have matured, the need for validation data has become obvious. Because of the difficulty in gathering in-pile data, there is very limited data useful for validation of the fracture initiation and propagation behavior predicted by these models.

Separate-effects validation experiments of fracturing fuel outside the reactor, but under thermal conditions comparable to those seen in the reactor, are being planned. Two out-of-pile experiments are proposed to create the necessary temperature gradient and associated stress to induce cracking. The first experiment set involves bulk heating of the pellet before sudden cooling from the pellet exterior. The second set of experiments employs resistive heating by applying a current through a fuel pellet to obtain heating similar to that caused by fission processes in the nuclear reactor. Both experiment designs are expected to produce a temperature profile with a parabolic shape and result in thermally-induced cracking similar to that observed under normal LWR operation conditions.

The focus of this thesis is to inform the design of the out-of-pile experiments so that relevant validation data is produced. To accomplish this goal, thermal mechanical models are established to evaluate the parametric variables. For the resistive heating experiment, temperature dependent electrical conductivity function was implemented to be used in calculating heat source term from Joule heating. The electrical module is coupled with thermal/mechanical modules.

Chapter 2

Background

2.1 Fuel Thermal Mechanical Performance

Ceramic uranium oxide was selected as fuel for light water reactors (LWRs) in the early 1950s [Olander, 2001]. Despite the fact that its thermal conductivity is much lower than other candidate fuels (Table 2.1), its compatibility with water and clad materials and the dimensional stability of UO_2 outweigh the conductivity weakness. However, this leads to a major challenge in heat removal, especially under severe accident conditions, and complicates fuel system design and optimizing fuel performance.

Table 2.1: Summary of material properties of uranium fuels, after [Rudling et al., 2007]

Property	Uranium	UO_2	UC	UN
Corrosion resistance in water	Very poor	**Excellent**	Very poor	Poor
Compatibility with clad materials	Reacts with normal clad	**Excellent**	Varies	Varies
Dimensional stability	Phase change at 665 and 770 ° C	Good	Good in lower atmosphere	Good (decomposes at 2600 ° C
Thermal conductivity, $W/cm \cdot K$	0.28 at 430°C	**0.03** at 1000°C	0.25 at 100 $\sim$ 700°C	0.2 at 750° C

Fuel pellets with the typical size of 1 cm in diameter are stacked within long cylindrical metallic fuel rods or cladding (Fig. 2-1). Zircaloy (or Zry) is usually used for cladding in LWRs due to its dimensional stability, small neutron cross section, chemical compatibility with UO_2 and water coolant, corrosion resistance and good mechanical properties. [Halabuk and Martinec, 2015]. The gap between fuel pellet and cladding, about 80 μm, is designed mainly to accommodate pellet swelling and radial thermal expansion during operation. The gap is back-filled with helium gas[1], which has a thermal conductivity much higher than air. The helium is pressurized to approximately 10 $\sim$ 20 atm to inhibit thermal conductivity reduction due to helium mixing with fission product gases (mainly Xe). The plenum, an

[1]Thermal conductivity of helium is 0.142 W/mK at 300 K, among the highest value of gases and 0.006 W/mK for Xe at the same temperature (from Eq. (9.18) in [Motta and Olander, 2017]).

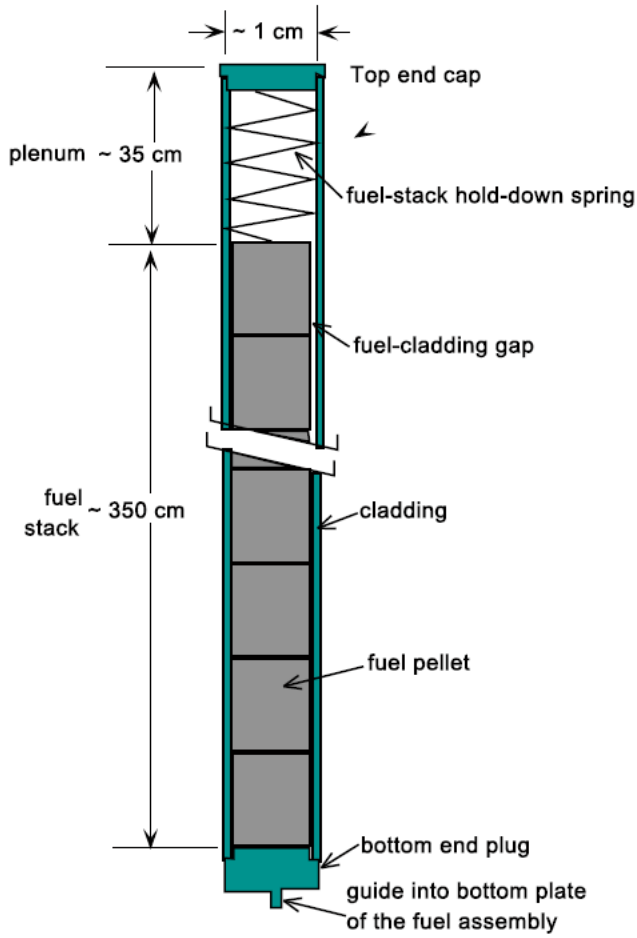

Figure 2-1: Fuel element [Olander, 2009]

open space above the pellets, is designed to contain fission product gases and prevent the cladding from being over pressurized. Heat generated in the pellet from fission is transferred from pellet to clad to the water coolant. In typical reactor operations, there is a slow increase in power to operating power (nominally 25 kW/m) over a long time (on the order of 10000 seconds). Under this condition, thermal behavior is essentially steady-state.

Even under steady state condition, fuel pellet behavior is very complicated. In modeling the behavior, one must consider multi-physics aspects (fully coupled nonlinear thermomechanics, chemistry, neutronics, thermal-hydraulics and mass transport) in multi-space (from microstructure to engineering scale) and multi-time (from rapid transient, short power ramps and long steady operation) scales. Mohr et al. [Rudling and Patterson, 2009] has shown the mechanisms (or processes) that occur in the fuel rod during normal operation. The re-

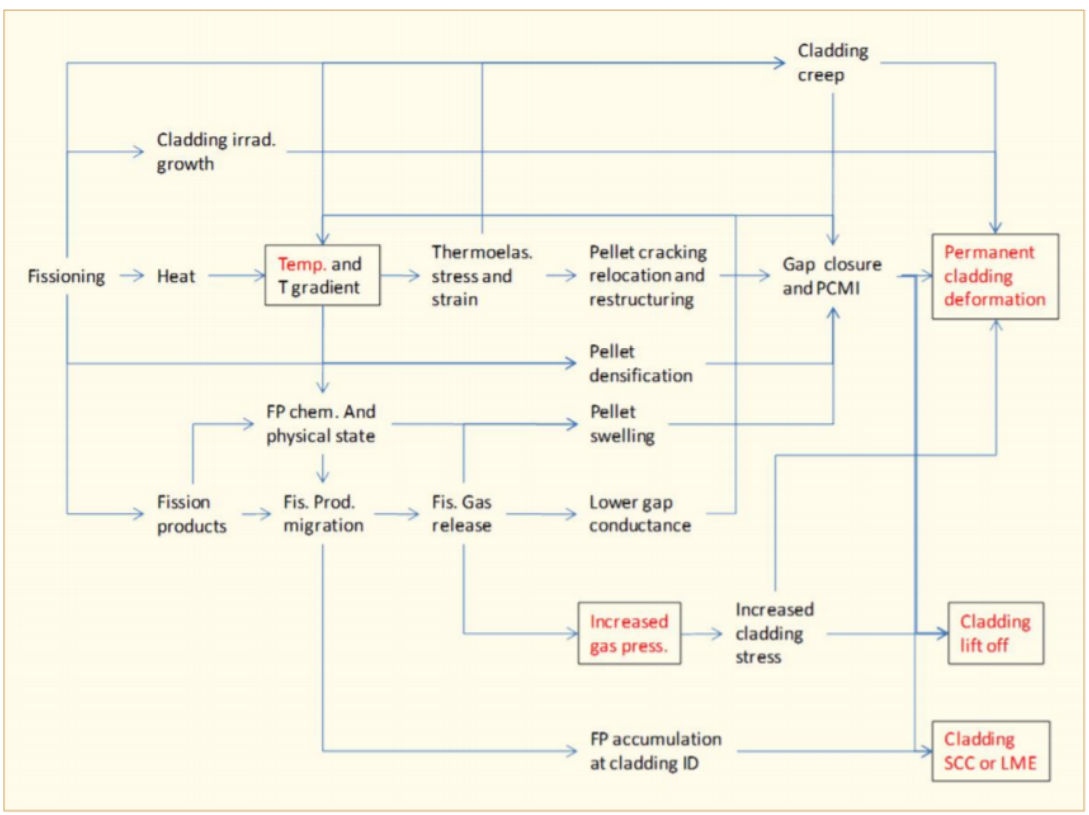

Figure 2-2: Essential processes taking place in the fuel rod and their interactions. (Mechanisms in red and contained in a box are key criteria for fuel design, [Rudling et al., 2007]).

lationship among the various processes are non-linear (Fig. 2-2). In this research, the main focus is on a subset of all the processes: $\boxed{Heat} \rightarrow \boxed{Temperature\ and\ Temperature\ gradient} \rightarrow \boxed{Thermoelastic\ stress\ and\ strain} \rightarrow \boxed{Pellet\ cracking}$ to study initial cracking and propagation during initial rise to power.

2.1.1 Fission and Heat

Fission is a process that occurs when certain heavy nuclei split into two smaller fragments upon absorption of a neutron (Fig. 2-3). Two or three neutrons, gamma rays, beta particles and energy are also released. Fig. 2-4 shows the mass number of the lighter fragment is around 95 and 140 for the heavier fragment for fission of ^{235}U. Approximately 200 MeV is released per fission. The power density is about 100 times more than in other sources [Zinkle and Was, 2013]. Ninety five percent of this energy is removed by the reactor coolant via conduction through fuel, gap and cladding. It is considered to be in a thermodynamic steady-state during normal operation at full power. The heat conduction equations in cylindrical coordinates is

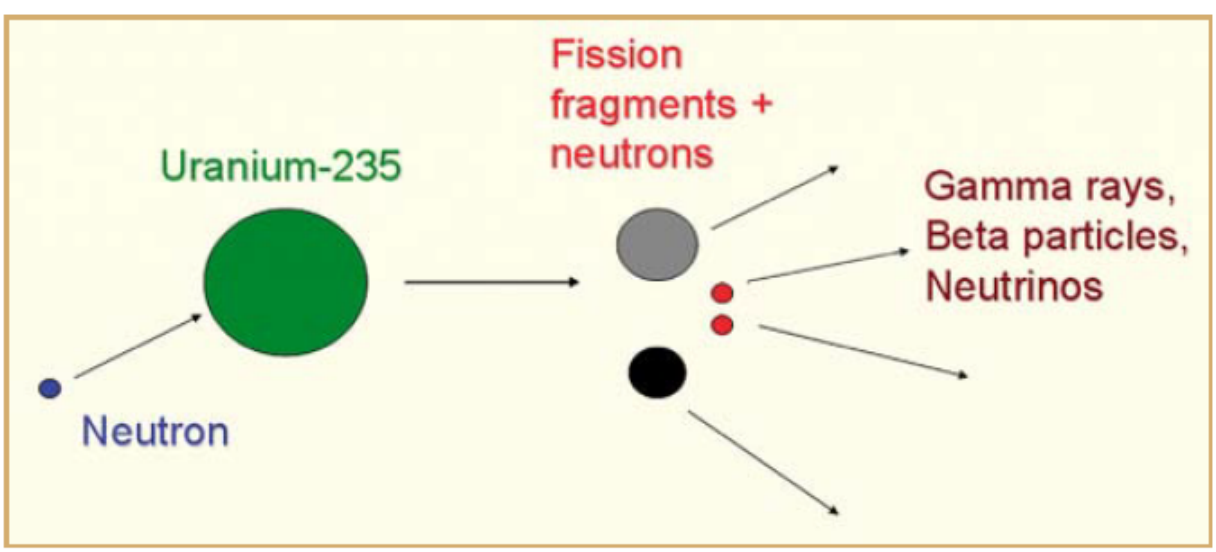

Figure 2-3: Fission process ([Rudling et al., 2007])

$$\frac{1}{r}\frac{d}{dr}\left(rk\frac{dT}{dr}\right) + Q = 0 \tag{2.1}$$

where

T is the temperature (K),

r is the radial position in the pellet (m),

k is the thermal conductivity ($W/m \cdot K$), and

Q is the volumetric heat generation from fission

$Q = 3.0 \times 10^{-11}\dot{F}$ in the pellet and

$Q = 0$ in the gap and cladding regions.

(190 MeV $\approx 3.0 \times 10^{-11} J$ and $\dot{F}$ is the fission rate density$[fission/m^3 \cdot s]$)

Boundary conditions are:

$$T(R_F) = T_s \tag{2.2}$$

where R_F is the fuel pellet radius (m) and T_s is the temperature on the pellet surface (K).

$$\left.\frac{dT}{dr}\right|_{r=0} = 0 \tag{2.3}$$

Assuming thermal conductivity is constant, the temperature profile in the fuel is parabolic, as shown in Eq. 2.4.

$$T(r) - T_s = \frac{QR_F^2}{4k}\left(1 - \frac{r^2}{R_F^2}\right) \tag{2.4}$$

2.1.2 Thermal Stress and Strain

Under real LWR normal operating conditions, parameters such as thermal conductivity and specific heat capacity of UO_2 and fuel-cladding gap width change with time. Fig. 2-5 shows

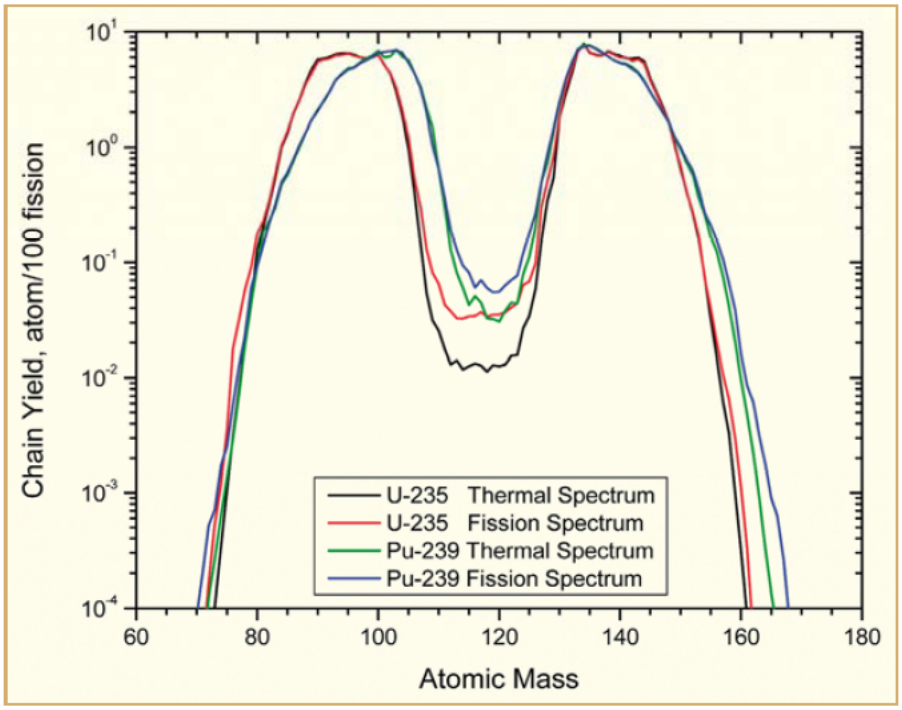

Figure 2-4: Fission products yield for U-235 and Pu-239 by neutron energy. [England and Rider, 1994]

the temperature distribution at different power levels at the beginning of life when fission gas being released and fuel burnup are negligible. The pellet center temperature is much higher than the pellet surface temperature and increases as power increases and the slope of the temperature profile near the surface becomes steeper as well. The surface film refers to the thermal boundary layer that exists when temperature on the cladding outer surface and the coolant temperature are different. Convective heat transfer occurs in this region, which is usually very narrow. The inner section of the fuel pellet experience compression due to greater thermal expansion at higher temperatures, compared to the outer regions which experiences tension (Fig. 2-6). Eq. 2.5 ([Motta and Olander, 2017, Eq. 9.30]) expresses the tangential (hoop) thermal stress in a pellet,

$$\sigma_\theta = -\frac{\alpha E q}{16\pi(1-\nu)\bar{k}}\left(1 - 3\frac{r^2}{R^2}\right) \tag{2.5}$$

where

σ_θ = Hoop stress (in the circumference direction), MPa,

E = Elastic modulus, MPa,

q = Linear power, W/m,

α = Thermal expansion coefficient, 1/K,

ν = Poisson's ratio

r = any position in radial direction in fuel

R = radius of fuel pellet, and

$\bar{k}$ = Average thermal conductivity, W/(mK).

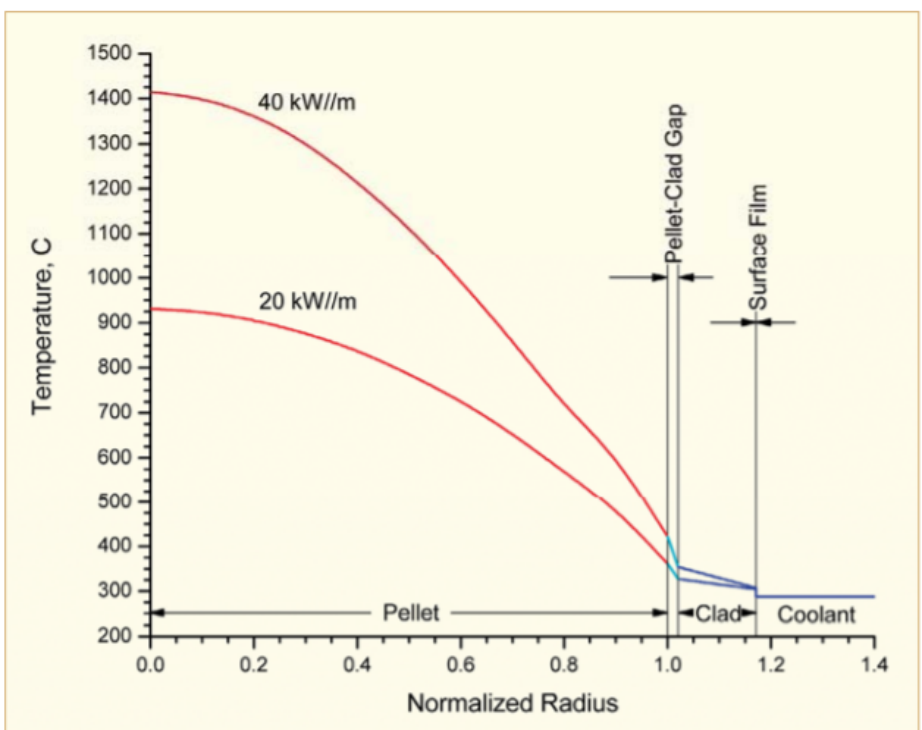

Figure 2-5: Temperature profile changes as power increases, at the beginning of the operation (from MATPRO equations) [Patterson and Garzarolli, 2010].

(a) The center portion of pellet is hotter and expands more, but is restraint by the cold outer region. Thus it experiences compression.

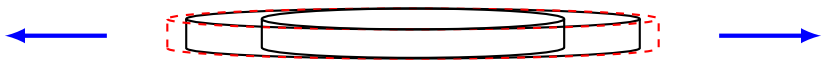

Figure 2-6: Pellet experiences compression in center and tension in outer region.

Using the data in Table 2.2, Eq. 2.5 indicates that the center 58 % of the pellet is under compression and the outer 42 % experiences tension (Fig. 2-7). Pellets crack when the internal stress exceeds the tensile strength. Simulations show that pellet cracking initiates at around 6 KW/m. Cracking initiates at the perimeter and propagates towards the pellet center as power increases (Fig. 2-8).

Table 2.2: Material properties of UO_2

Material properties	
Thermal conductivity $\bar{k}$	5 W/(mK)
Fracture strength	150 MPa
Thermal expansion coefficient, α	10^{-5} /K
Young's modulus	2×10^5 MPa
Poisson's ratio	0.345

2.1.3 Gap Closure and Pellet-cladding Interaction

Pellets having an hourglass or wheat sheaf shape ([Olander, 2009]) were found after just one reactor cycle because there is no constraint at the top and the bottom edge of the pellet and thermal expansion is greater than in the middle of the pellet. The gaseous and solid fission product formation also contribute to fuel swelling. Both thermal stress induced cracking and swelling cause gap closure, and subsequent pellet-cladding interaction(PCI) at both ends of

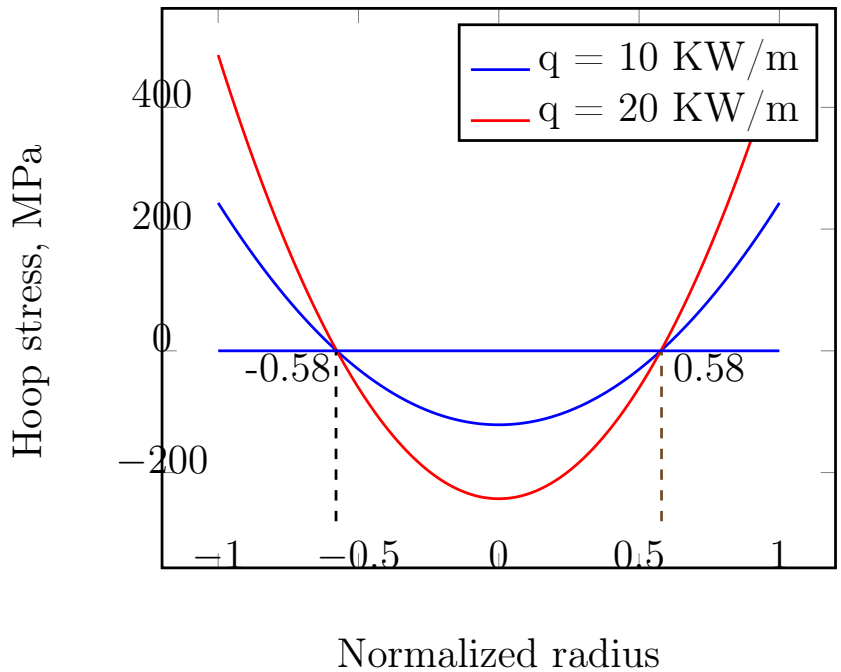

Figure 2-7: Hoop stress profile at q = 10 KW/m (blue line) and 20 Kw/m (red line) in Eq. 2.5

pellets [2]. The edges of pellets can then push cladding outward (bambooing). The stress state of these contact points is high. As cladding becomes brittle, high stress concentration may cause initial cracking on the inner cladding surface. Fig. 2-9 shows stress corrosion crack of clad due to a chipped pellet surface. The gap between pellet and clad is wider due to the missing piece of fuel. Gap conductance reduces, thus the local temperature rises. When there is a fuel crack nearby, fission products have paths to rapidly reach crack tips in cladding. Fission products may react with zirconium in cladding to form brittle compounds, such as ZrI_4, which ruptures easily. Both cladding embrittlement and stress-corrosion can lead to cladding failure.

The high temperature gradient caused by high energy output from fission and the low thermal conductivity of UO_2 are the key elements resulting in fuel cracking. A better understanding of the factors affecting the temperature profile change within a fuel pellet from the early

[2]Gap closes after 1 year with 80 μm gap [Olander, 2009].

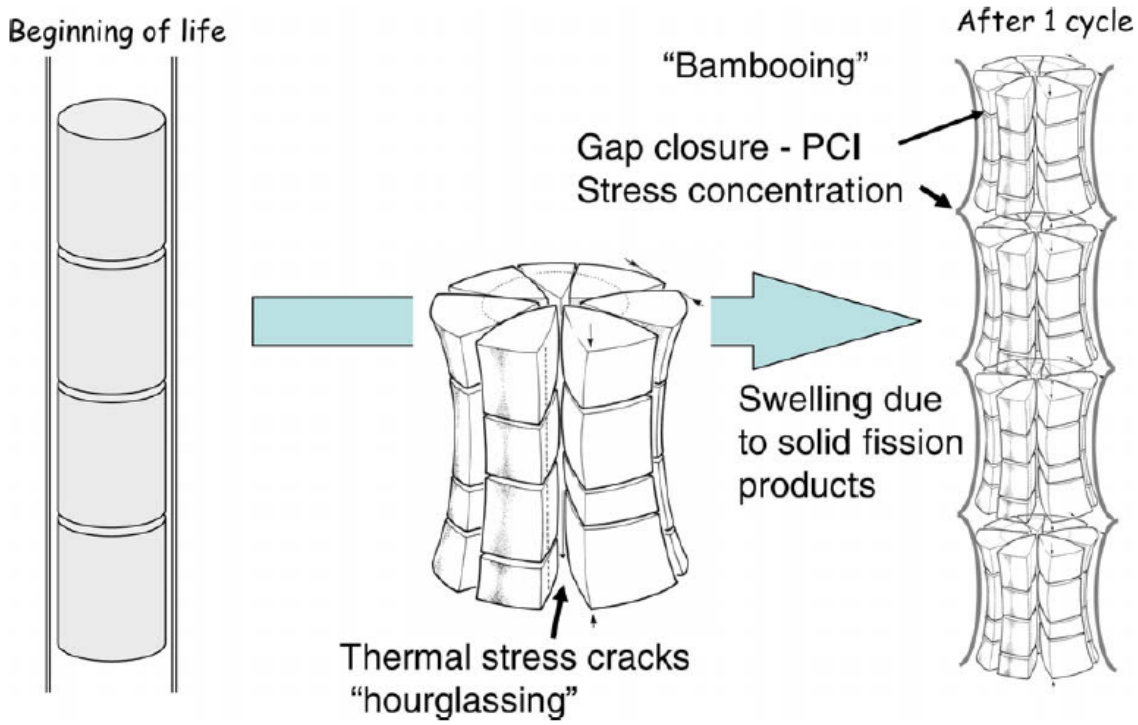

Figure 2-8: Hourglass shape and bambooing induced by thermal expansion, fission product swelling and thermal stress cracks [Olander, 2009].

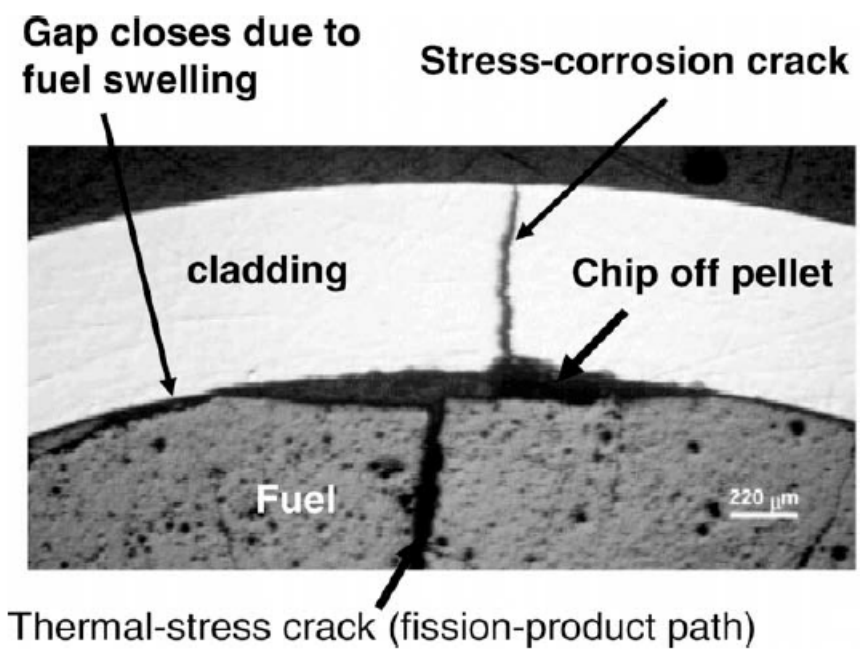

Figure 2-9: Stress corrosion crack leads to cladding failure [Olander, 2009].

stage is crucial to evaluate fuel performance, safety and fuel design.

2.2 Bison fuel performance code

The Bison fuel performance code [Bison, 2018, Williamson et al., 2012, Hales et al., 2013, 2015] is used for the fuel fracture simulation in this research, which has been developed at Idaho National Laboratory (INL) since 2009. Bison is built on MOOSE (Multiphysics Object Oriented Simulation Environment Gaston et al. [2009]) which utilizes the Jacobian-free Newton-Krylov (JFNK) method for solving fully coupled nonlinear partial differential equations. The physics models in MOOSE are modularized as kernels, which facilitates including new material models and coupled physics. Bison can simulate steady state and transient behavior for a single fuel rod in 1D spherical, 2D axisymmetric or 3D geometries. It solves thermal mechanics equations with species diffusion in a tightly coupled manner. Even though fission gas production and burnup are built in to Bison, they are excluded in this study on fresh fuel fracture during start up. Unlike dimensional independent physics in MOOSE, SI units are utilized in Bison as built-in empirical models are using the SI system.

2.2.1 Materials Properties

2.2.1.1 Heat Capacity and Thermal Conductivity ofUO_2

Fink-Lucuta ([Fink, 2000]) models for temperature dependent thermal conductivity and specific heat were used in this research, for the temperature range 298 K to 3120 K. Generally speaking, lattice vibration (phonon conduction) and electrical conduction are the two contributions to thermal conductivity, k, for fresh fuel at 95 % theoretical density (TD) UO_2. Thus,

$$k_{95} = k_{phonon} + k_{electronic}$$

where

$$k_{phonon} = 1.0/(A + B * T + f(Bu) + g(Bu) * h(T))$$

and

$$k_{electronic} = i(T) * exp(-F/T)$$

where

A, B, F are constants,

Bu is burnup, and

f, g, h, and i are functions.

Fink's curve fitting model for k_{95} (Fig. 2-10) is

$$k_{95} = \frac{100}{7.5408 + 17.692t + 3.6142t^2} + \frac{6400}{t^{5/2}} \exp\left(\frac{-16.35}{t}\right) \tag{2.6}$$

where

t = T/1000 in K and

k is thermal conductivity in W/mK.

The overall thermal conductivity expression including correction factors is

$$k = k_{95} * f_d * f_p * f_{por} * f_x * f_r$$

where

f_d is dissolved fission products correction,

f_p is precipitated fission products correction,

f_{por} is porosity correction,

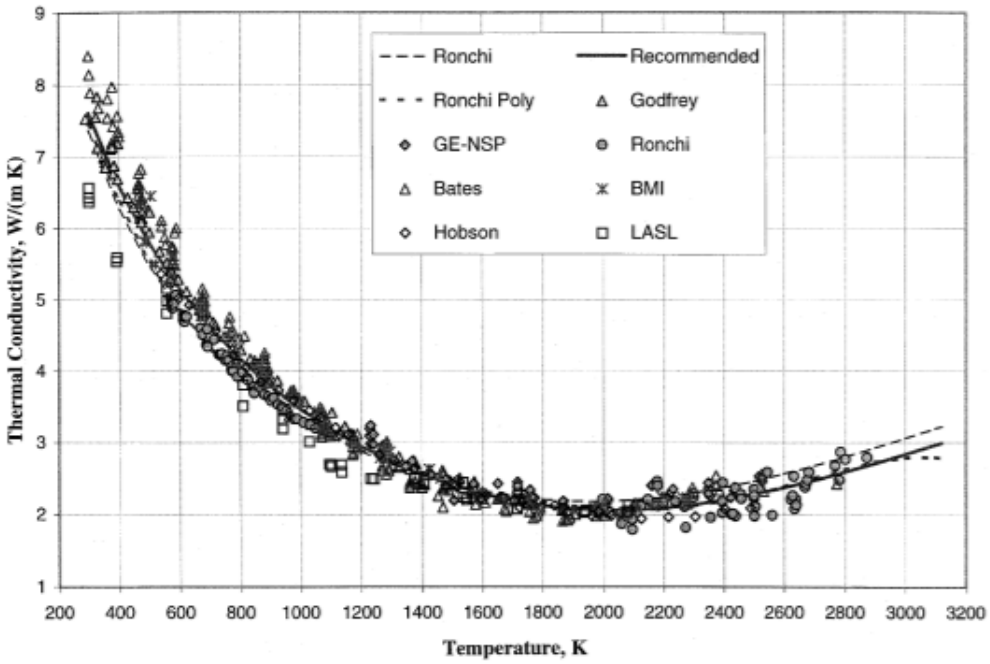

Figure 2-10: Thermal conductivity of unirradiated UO_2 from different data

f_x is the deviation from stoichiometry and

f_r is the radiation damage correction.

and heat capacity C_p ,

$$C_p(T) = 52.1743 + 87.951t - 84.2411t^2 + 31.542t^3 - 2.6334t^4 - 0.71391t^{-2}$$

2.2.1.2 Constant Material Properties

Constant materials properties of UO_2 and Zircaloy cladding in LWR are summarized in Table 2.3.

Table 2.3: Constant material properties used in simulations.

Material property	UO_2	Zircaloy
Density (Kg/m^3)	10431	6551
Thermal conductivity (W/mK)	built-in	16
Heat Capacity, c_p, $(J/(Kg \cdot K)$	built-in	330
Young's modulus (MPa)	2×10^5	built in
Poisson's ratio	0.345	built-in
Thermal expansion coefficient (1/K)	10^{-5}	7.2×10^{-6}

2.2.2 Gap conductance

Calculation of overall gap conductance in Bison combines the effects of gas conductance, conductance from pellet-cladding contact and from radiant heat transfer between pellet surface and the cladding inner wall.

$$h_{gap} = h_g + h_s + h_r$$

where

h_{gap} is the overall gap conductance,

h_g is the gas conductance,

h_s is conductance due to solid-solid contact and

h_r is the conductance due to radiant heat transfer.

The gas conductance relation and solid conductance model are suggested by Ross and Stoute [Ross and Stoute, 1962]:

$$h_g = \frac{k_g}{d_g + C_r(r_1 + r_2) + g_1 + g_2} \tag{2.7}$$

where

k_{gas} is the gas conductivity in the gap,

dg is the calculated corresponding gap width via solid mechanics,

C_r is a roughness coefficient with r_1 and r_2 the roughness of the two surfaces, and

g_1 and g_2 are jump distances at the two surfaces.

and

$$h_s = C_s \frac{2k_1k_2}{k_1 + k_2} \frac{P_c}{\delta^{1/2} H} \tag{2.8}$$

where

$C_s = 10m^{-1/2}$, an empirical constant,

k_1 and k_2 are the thermal conductivities of fuel pellet and cladding,

P_c is the constant pressure,

$\delta = 0.8(r_1 + r_2)$, the average gas film thickness, and

H is the Meyer hardness of the softer material.

The radiant conductance is obtained from the diffusion approximation based on the Stefan-Boltzmann Law:

$$q_r = \sigma F_e (T_1^4 - T_2^4) \approx h_r (T_1 - T_2) \tag{2.9}$$

Therefore,

$$h_r \approx \frac{\sigma F_e (T_1^4 - T_2^4)}{T_1 - T_2} = \sigma F_e (T_1^2 + T_2^2)(T_1 + T_2) \tag{2.10}$$

where

σ is the Stefan-Boltzmann constant,

T_1 and T_2 are the temperatures of the radiant surfaces and

$F_e = \frac{1}{\epsilon_{eff}} = \frac{1}{1/\epsilon_1 + 1/\epsilon_2 - 1}$ is an emissivity function for infinite parallel plates with emissivities ϵ_1 and ϵ_2 of the radiating surfaces and the effective emissivity ϵ_{eff}.

2.2.3 Gap/pleunum temperature and pressure

Since the gap and plenum are not meshed, the approximate temperature in the gap and plenum area is the average temperature of the pellet surface and cladding inner surface.

$$T = \frac{T_o + T_i}{2}$$

Calculation of the pressure in the gap/plenum region is based on the ideal gas law:

$$P = \frac{nRT}{V}$$

where

P is the pressure in gap/plenum,

n is the number of moles of gases,

R is the ideal gas constant,

V is the volume and

T is the temperature.

The number of moles (n) includes original helium and later fission gas generated during fission. The gap size changes as well due to pellet thermal expansion, cracking and fission product swelling.

2.3 Fracture Models

Several models for fuel fracture have been developed using various theories based on different criteria. Each has benefits and drawbacks. Extended finite element methods, Peridynamics

and phase field methods have all been implemented in the Bison code, and should be validated. The fixed smeared cracking model is used in experiment design for it is relatively easy of use.

2.3.1 Smeared Cracking Model

The fixed smeared cracking model [Rashid, 1968] is used in this simulation for its ease of use. The concept is based on the linear elastic constitutive laws for brittle ceramic materials, followed by a softening stress-strain law to modify the elastic constants at mesh nodes after cracking. When a principle stress is greater than the fracture stress, a crack in that direction at the material point is initiated and the stress is set to zero. The direction of the propagation of the crack is fixed by the original principle direction. However, mesh sensitivity with respect to crack orientation and size is a major drawback.

2.4 Approach to Simulations

For validation purposes, the model needs to incorporate the physics of the experiments. To study the crack initiation and growth during LWR rise to power, several tests are planned to represent different levels of cracking as in LWR; therefore, simulation of LWR operation during first rise to power was conducted to get the equivalent power level for out-of-pile experiments for comparison purposes.

Two major criteria for out-of-pile experimental design are alternate heat source to replace fission and high heat removal rate ($\sim 70 \times 10^6 Kg/hr$ in LWR) to create large temperature gradient and associated high hoop stress on the fuel surface. To translate the full scale in-reactor phenomena to a single pellet in a controlled environment in the laboratory is challenging. Thus the main goal of this research is to focus on modeling the proposed out-of-pile experiments and running simulations to identify key factors in the out-of-pile experiments

to replicate the thermal conditions and narrow down the parameter range needed to produce useful output. By working with the experimental teams closely, the experimental results will give us meaningful insight to improve and validate the fracture models.

Chapter 3

Thermal Shock

3.1 Background

Ceramics are typically used in high temperature applications because they have high melting temperatures and can withstand high heat. However, the brittleness and low thermal conductivity of ceramics can cause fracturing under severe thermal transient conditions. Therefore, thermal shock damage of ceramics has been studied for over a century. It becomes more important to understand thermal shock behavior as technology improves, more advanced and sensitive ceramic devices are developed, and ceramics are used in harsh environments. Thermal stress induced cracking model (Eq. 3.1) was one of the original methods to approach initial cracking based on thermoelastic theories when the thermal stress is slightly greater than the tensile strength of the material (Eq. (2) in [Wang and Singh, 1994]).

$$\Delta T_c = \frac{\sigma_t(1-\nu)}{\alpha E} = R \tag{3.1}$$

where

ΔT_c is the critical temperature difference to cause initial cracking,

σ_t is the material's tensile strength,

ν is the Poisson's ratio of the material,

α is the thermal expansion coefficient,

E is the Young's modulus and

R is the thermal shock resistance

For most ceramic applications, testing is focused on the thermal shock resistance of the material at temperatures above the normal operational temperature range. In this research, thermal shock experiments are being explored as options to create higher temperature gradients across a fuel pellet that replicate reactor operating conditions and induce thermal cracking. UO_2 pellets are heated in a hot bath until they reach the equilibrium state, then submerged in a cold bath. The biggest challenge for experiment design is to produce a temperature gradient large enough to cause cracking without an internal heat source.

3.2 Experiments

In the proposed experiment, a UO_2 ceramic pellet will be heated in a molten salt "hot bath" until the pellet reaches equilibrium. Then the pellet will be plunged into a "cold bath" to cause the pellet surface temperature to decrease quickly. The experiment objective is to create a steep temperature profile near the pellet edge. The pellet will be placed in a cladding-like vessel for heating and cooling to avoid any reaction between UO_2 and the baths. Standard 5/8" copper tubing is used to create this vessel. Similar to the fuel rod in an LWR, the gap between fuel and cladding is necessary to accommodate thermal expansion and cracking of the pellet. While the gap is necessary, it is also important to fill the gap with a medium that allows the fuel expansion but also conducting heating between the pellet and clad. If the thermal conductivity of the medium is too low, there is insufficient heat removal from the pellet surface to create the desired radial temperature gradient near the pellet surface. Initial modeling efforts for this thesis were conducted to determine the

effect of gap thermal conductance. The result of this effort was a modification of experiment design from using a gas in the gap to wrapping copper foil around the pellet (approximately 12 revolutions to fill 80% of the gap) to improve heat transfer across the gap. The effect of thermal conductance in the gap is discussed in more detail in section 3.4.1.

The detailed dimensions of the UO_2 pellets, copper wrapping foil, copper holding tube and copper rod (used in preliminary testing in place of the UO_2 pellet) are listed in Table 3.1. A pellet assembly is heated in a hot salt bath held at 873 K. When the fuel pellet center temperature reaches 873 K, the assembly is submersed in a cold bath (270 K) comprised of a 50/50 mixture of ethylene glycol and water. This solution is selected to provide a larger temperature range for the experiments. However, this mixture has a lower heat transfer rate than pure water.

Table 3.1: Thermal Shock experiment dimensions

(a) Pellet dimensions

Pellet	Diameter (mm)	Gap (mm)
Surrogate pellet (Cu rod)	12.97	0.74
UO_2 pellet	11	1.725

(b) Copper holding tube (standard 5/8" tubing)

Inner diameter (mm)	14.45
Outer diameter (mm)	15.875
Wall thickness (mm)	0.7112

(c) Copper foil (gap fill)

Multipurpose 110 copper sheet, softened temper	
Width (mm)	12.7
Thickness (mm)	0.0508

3.2.1 Leidenfrost effect

As the testing assembly is heated to 873 K, The Leidenfrost effect has been observed when the heated assembly (at 873 K) is first immersed in the cold bath. The Leidenfrost effect, discovered by Johann Gottlob Leidenfrost in 1756, is a phenomenon that when a small amount of liquid is in contact with a large mass of a hot object (object temperature is much higher than the boiling point of liquid), the liquid vaporizes immediately and forms an insulating vapor layer between the hot solid surface and the liquid. As large slow moving bubbles form, radiant heat transfer becomes more significant at high excess temperature. This phenomenon reduces heat transfer from the hot solid surface to the cold liquid. The heat transfer coefficient including the Leidenfrost effect for vertical tubes is approximated using the following equation by Hsu and Westwater [Welty et al., 2007],

$$h\left(\frac{\mu_v^2}{g\rho_v(\rho_L-\rho_v)k_v^3}\right)^{1/3} = 0.0020\left(\frac{4\dot{m}}{\pi D_o\mu_v}\right)^{0.6} \tag{3.2}$$

where

$\dot{m}$ is the mass flow rate in lb_m/hr at the upper end of tube,

μ_v is the vapor viscosity,

g is gravity,

ρ_v is the density of the vapor,

ρ_L is the density of the liquid,

k_v is the thermal conductivity of the vapor, and

D_o is the outside diameter of the vertical tube

Eq. (3.2) was recommended for a vertical tube as heat transfer rates for vertical tubes are higher than that on a horizontal plate.

3.2.2 Schematics

The configuration of pellet-clad assemblies for the Cu surrogate and UO_2 pellets are illustrated in Fig. 3-1.

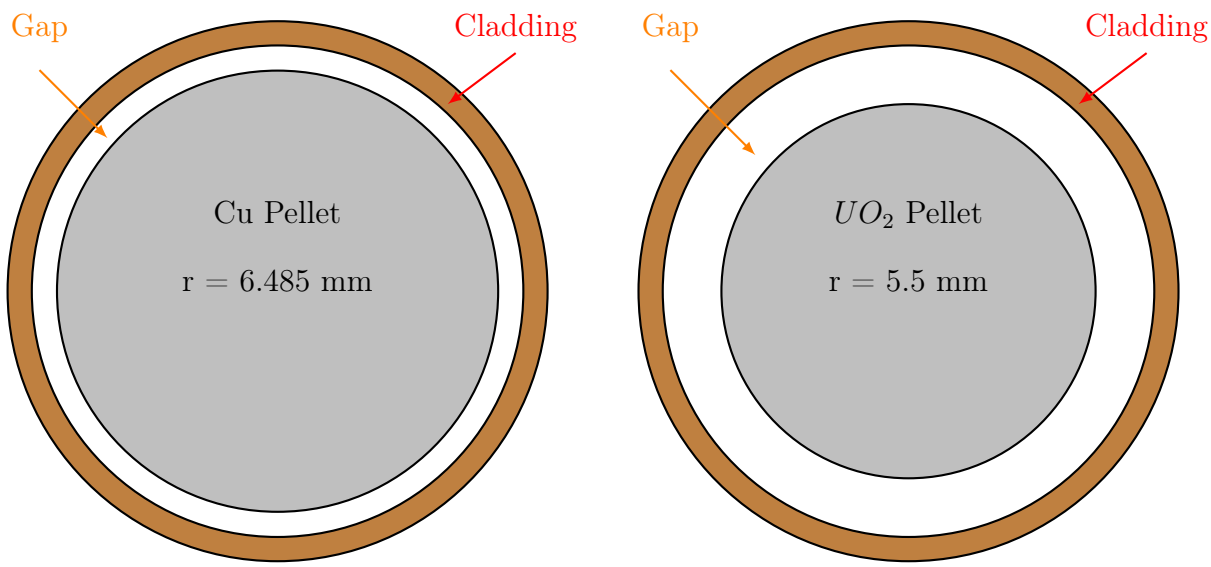

(a) Cu surrogate pellet (b) UO_2 pellet

Figure 3-1: Cross-sections of the proposed thermal shock experiment using Cu and UO_2 pellets in standard 5/8" copper tubing

3.3 Governing Equations

The equations describing the physical parameters of the experiments are presented in this section. The heat equation without heat source is:

$$\rho C_p \frac{\partial T}{\partial t} - \nabla \cdot q = 0$$

where the heat flux is:

$$q = k \nabla T$$

Initial condition:

$$T(r, 0) = T_i$$

Boundary condition:

$$k\frac{\partial T}{\partial r}\Big|_{r=R} = h(T_\infty - T_R)$$

where

T is the temperature (K),

ρ is density (Kg/m^3),

C_p is specific heat ($J/Kg \cdot K$),

k is thermal conductivity ($W/m \cdot K$) of the material,

T_i is the initial temperature (K),

R is the cladding outer diameter,

h is the convective heat transfer coefficient ($W/m^2 \cdot K$),

T_∞ is the temperature of the cold bath and

T_R is the cladding outer surface temperature.

Momentum conservation at static equilibrium

$$\begin{aligned} \nabla \cdot \sigma &= 0 \\ \sigma &= E\epsilon \\ \epsilon &= \nabla_s u + \alpha \Delta T \\ \nabla_s u &= \frac{1}{2}(\nabla u + \nabla u^T) \end{aligned} \tag{3.3}$$

where

σ is the Cauchy stress tensor,

α is the thermal expansion coefficient (1/K),

$\nabla_s u$ is the strain rate tensor and

u are the displacements.

There is neither heat source nor external body force. Samples are heated in a hot bath at temperature, T_i. Because UO_2 is a brittle material, stress and strain is in the elastic region of the stress vs strain curve. Thermal expansion is included as the temperature gradient is high.

3.4 Results and Discussion

Assumptions:

- Tensile strength is assumed to be 150 MPa for fresh fuel
- Materials are homogeneous and isotropic
- Young's modulus of copper foil is set to 1 Pa since it is wrapped around the pellet and fills about 80 % of the gap. It is free to expand when pushed by pellet expansion and fracture.
- Due to the significant gap size, gap is meshed and the specific heat capacity is calculated by using the rule of mixtures. Thus $C_{p,gap} = 0.8 * C_{p,Cu} + 0.2 * C_{p,air}$.

3.4.1 Gap Materials Selection

As the dimensions of the assembly are developed, there are two unknown variables: thermal conductance in the gap and convective heat transfer coefficient of the ethylene glycol/water solution and copper tube. The values of these affect the radial temperature gradient near the pellet surface; if the heat transfer is too slow, no cracks will be observed. Simulations were run with a range of the two unknowns.

Because of the large gap and the limitation of gap medium options due to the reactivity of UO_2, this step narrows down the medium options while incorporating the key experiment parameters. The primary purpose of ethylene glycol is to lower the freezing point of the solution; however, its specific heat capacity is only one half of pure water. Thus, the overall heat transfer rate between the copper tube and the cold bath is lower than if water were the coolant. The fracture strength of UO_2 is approximately 150 MPa, and Fig. (3-2) summarizes the shock (the temperature difference between hot bath and cold bath) needed for the hoop stress to approach the fracture point (initial cracking). Since the thermal conductivity of UO_2 is between 2 to 7 W/mK and the convective heat transfer coefficient of still water is 500 W/m^2K, simulations were conducted using mediums with thermal conductivity ranging from $0.75 \sim 30$ W/mK for three cases with convective heat transfer coefficients equal to 400, 500, and 1000 W/m^2K.

For all three cases, a large shock is required when the thermal conductivity, k, in the gap is under 2 W/mK. The shock needed decreases as k increases from 2 to approximately 10 W/mK and stabilizes at k-values greater than 10 W/mK. This is because the gap size is relatively large (1725 μm, compared with regular gap size of 80 μm), and the effect from gap conductance becomes more significant. The thermal conductivity of UO_2 is between $2 \sim 7$ W/mK, and when the thermal conductivity of the gap is less than UO_2, heat inside the pellet redistributes and the temperature reaches the average faster than when the heat transfer rate out of the pellet is lower. A larger shock is necessary to create the desired temperature gradient so that hoop stress is higher than fracture strength. When the thermal conductance of the gap is greater than that of UO_2, heat transfer near the pellet surface is higher than the heat transfer from pellet center to the surface, which produces the temperature gradient needed for fracture initiation to occur.

Although the effect of gap size on heat transfer is quite large, heat transfer from the copper

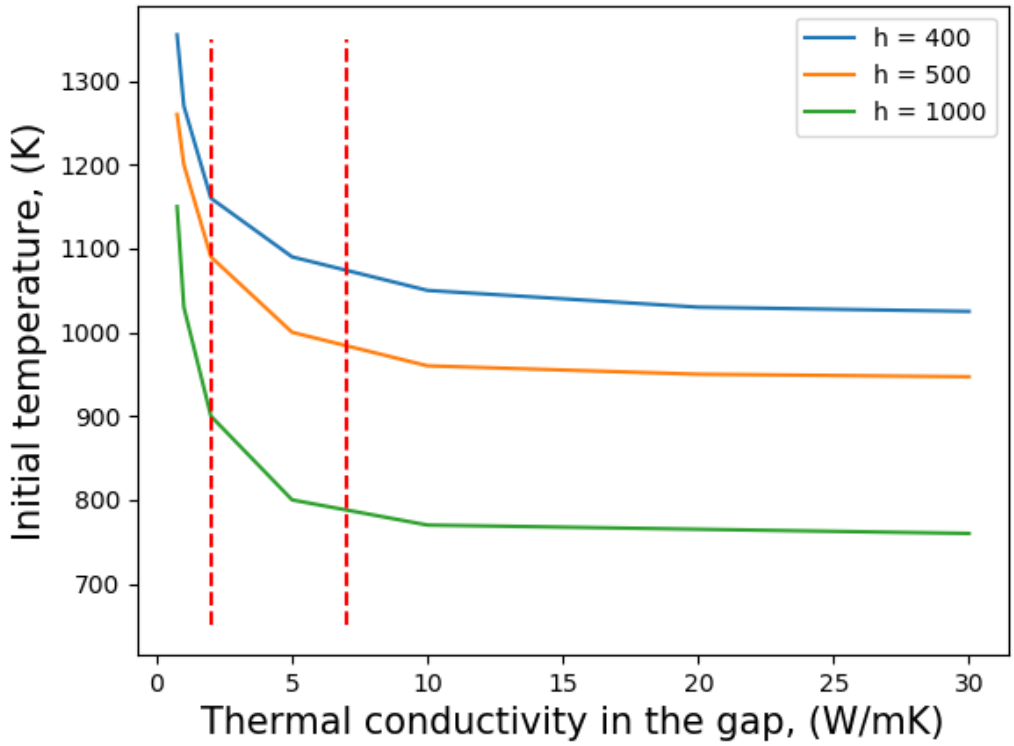

Figure 3-2: Initial temperature required for hoop stress to reach 150 MPa on the pellet surface when quenched into a cold bath at $-3°C$ with different levels of thermal conductivity in the gap and coolant convective heat transfer coefficient (h). The thermal conductivity of UO_2 is 2 to 7 W/mK, indicated in the red dashed lines.

tubing to the cold bath also plays a big role. The required initial temperature lowers about 70 degrees when h changes from 400 to 500 W/m^2K and 140 degrees when h changes from 500 to 1000 W/m^2K. The total effect of gap conductance and coolant heat transfer coefficient can be interpreted in the overall heat transfer coefficient U [Incropera and DeWitt, 2011] (to simplify it, 1D - steady state equation is demonstrated here and constant material properties and constant gap and cladding width are used).

$$\frac{1}{U} = \frac{d_{gap}}{k_{gap}} + \frac{d_{clad}}{k_{clad}} + \frac{1}{h_{cold}} \tag{3.4}$$

where

d_{gap} = 0.001725 m, the gap width,

d_{clad} = 0.0007125 m, cladding thickness,

k_{gap} is the thermal conductivity in the gap,

k_{clad} = 110 W/mK, the thermal conductivity of the copper tubing, and

h_{cold} is the heat transfer coefficient of cold bath.

The cladding term is negligible compared to the other two terms. For the different values of gap conductance and coolant heat transfer coefficient, the overall U can be calculated from Eq. 3.4. Fig. 3-3 shows initial temperature required to reach the fracture threshold 150 MPa vs overall U. The second order polynomial $T = 0.0012U^2 - 2.0758U + 1663.6$ accounts for 99.37 % of the variance. This simple 1-D overall heat transfer coefficient equation can be used for estimating the necessary shock for crack initiation.

3.4.2 Case Studies

While the experiment setup was under development, cases were investigated for the possible parameters (h_{cold} and k_{gap}) for the cracking development. The following simulation tests were all first raised to 873 K the first second then quenched to 228 K. Three cases were considered here to demonstrate that cracking patterns occurring at different power levels in LWR can be achieved by adjusting the convective heat transfer coefficient, h, and fixed gap thermal conductivity at 10 W/mK. A fourth case using a gap conductance of 380 W/mK (the thermal conductivity of copper foil), to show how the experiment would behave with a significantly improved thermal conductivity of the gap medium, was also considered. The results are shown in the temperature profile at the highest temperature gradient, maximum hoop stress, and crack pattern when cracking stops.

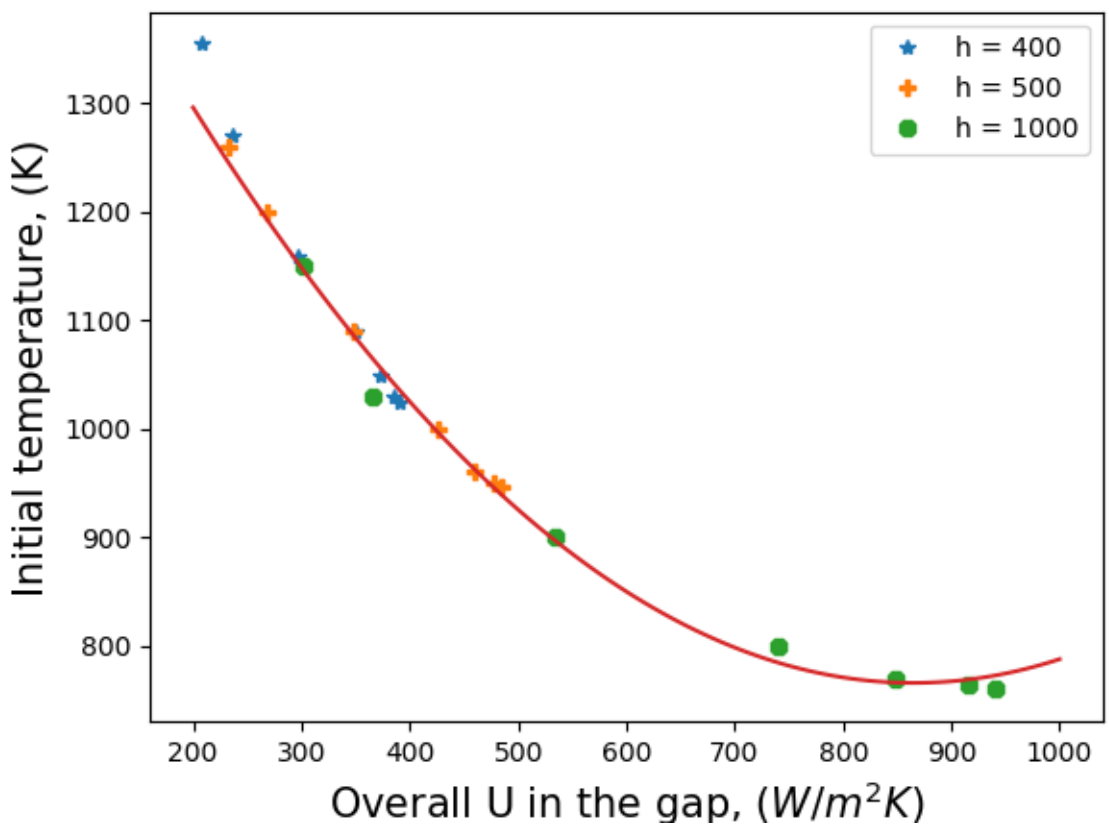

Figure 3-3: Initial temperature required to obtain the fracture threshold in terms of overall heat transfer coefficient (defined in Eq. 3.4). Polynomial fitting: $T = 0.0012U^2 - 2.0758U + 1663.6, \quad R^2 = 0.9937$

3.4.2.1 Case study 1: h = 750 W/m^2K and k_{gap} = 10 W/mK, quenched to $-45°C$

Fig. 3-4a shows the evolution of the centerline and surface temperature over time and the difference between the two. The maximum temperature difference is 135 degrees at 5.5 sec. The temperature drops from the surface towards the center (Fig. 3-4b). The center temperature is 845 k at 4 seconds when the temperature gradient on the pellet surface is a maximum. Hoop stress on the surface reached a maximum of 156 MPa at 3 seconds (Fig. 3-6a) and four cracks initiated at 4 seconds (Fig. 3-5). Centerline hoop stress distribution changes (in transient state) similar to Fig. 2-7 in steady state: compression in the inner core and tensile in the outer region. Since this is the transient state, the zero stress point is not at the same location as in the steady state. The hoop stress reaches 150 MPa fracture

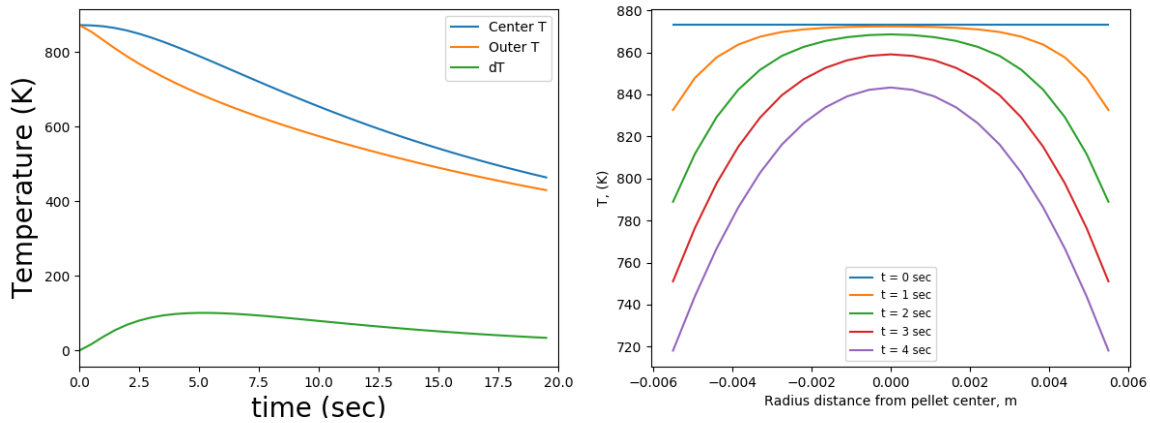

(a) Center and surface temperature change history

(b) Temperature profile time history.

Figure 3-4: Thermal shock result when quenched from 873 k to 228 K, $h = 750\ W/m^2K$ and $k_{gap} = 10W/mK$.

threshold at 3 seconds and reduces on the left side due to crack initiation at t = 4 sec (Fig. 3-6b).

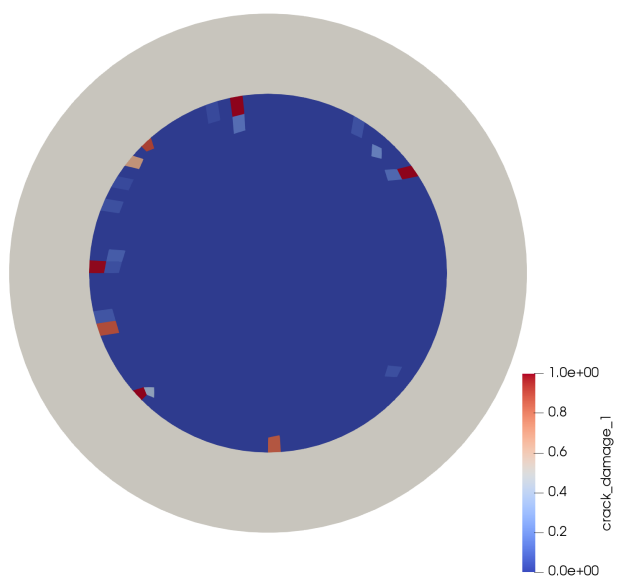

Figure 3-5: Crack initiated at 4 seconds. (Cracking damage index: 0 = undamaged; 1 = damaged). Simulated result for pellet quenched from 873 k to 228 K, with $h = 750\ W/m^2K$ and $k_{gap} = 10W/mk$.

Radial displacement on the pellet surface is at the maximum, 32.8 μm, at 0.5 sec and gradu-

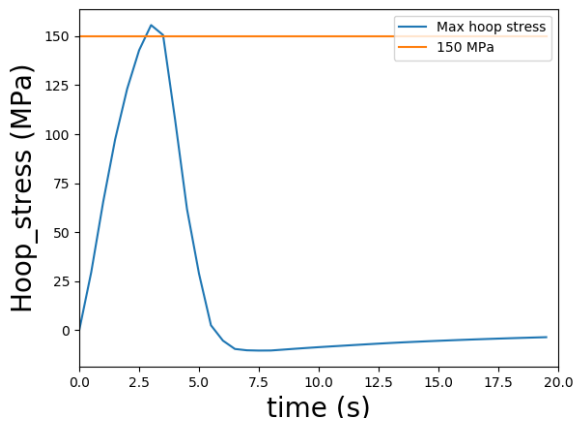

(a) Maximum hoop stress time history

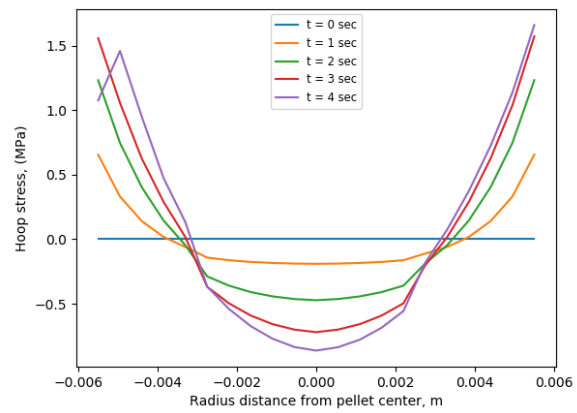

(b) Hoop stress profiles time history.

Figure 3-6: Hoop stress in pellet when quenched from 873 k to 228 K, with $h = 750\ W/m^2K$ and $k_{gap} = 10W/mk$.

ally declines with time (Fig. 3-7a). Fig. 3-7b illustrates that radial displacement transitions along the horizontal centerline, slightly differing between the left end point (28.6 μm) and right end point (28.2 μm) due to crack initiation. Because there is no internal heat source in these experiments, the driving force is from the thermal shock (temperature difference between initial pellet temperature and cold bath temperature). This difference reduces as the pellet temperature reaches equilibrium with the cold bath temperature. Thus, cracking progresses for about 4.5 seconds then stops (Fig. 3-10). To compare these simulated experimental results with behavior of fuel pellets in an LWR, the temperature gradient near the pellet surface is considered with respect to the normalized pellet radius (r/r_0), where the initial radius, r_0, for the experimental pellets is 5.5 mm versus 4.1 mm for commercial LWR pellets. Fig. 3-9 illustrates the correlation between the r/r_0 to temperature curve for the experiment results and the LWR behavior at 8 kW/m. The simulated fuel damage pattern at that power level in an LWR is shown in Fig. 3-11. Cracking occurs for 3.5 seconds and the crack length is about 17 % of the pellet diameter. This pattern is comparable to the fuel cracking pattern in an LWR at 8 kW/m.

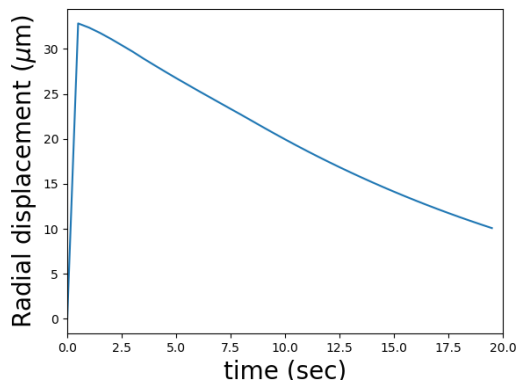

(a) Surface radial displacement history, maximum at 0.5 sec.

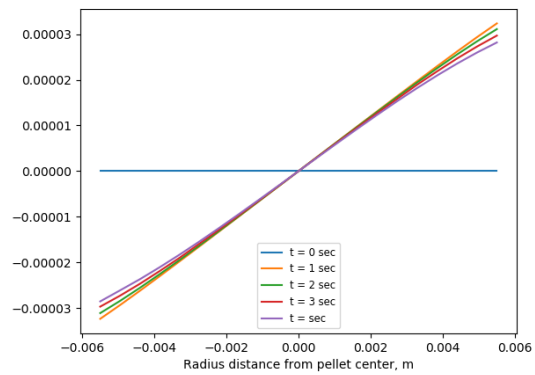

(b) Centerline displacement time history.

Figure 3-7: Displacement in pellet when quenched from 873 k to 228 K, with $h = 750$ W/m^2K and $k_{gap} = 10W/mk$.

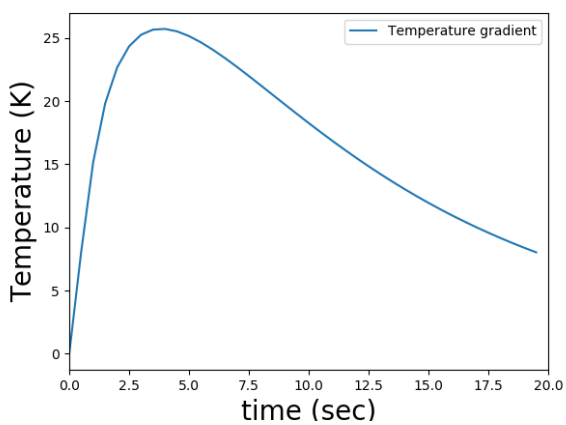

Figure 3-8: Time history of the temperature gradient on the surface

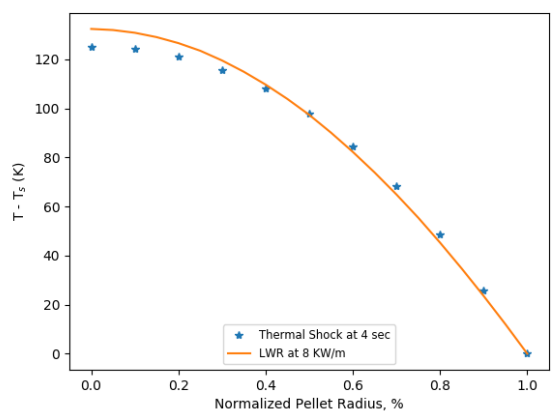

Figure 3-9: Comparison of surface temperature gradient for thermal shock experiment and LWR

3.4.2.2 Case study 2: h = 1000 W/m^2K and k_{gap} = 10 W/mK, quenched to $-45°C$

The convective heat transfer coefficient, h, was increased to 1000 W/m^2K in the second case study. Fig. (3-12a) shows the maximum temperature difference between the pellet centerline and surface is 161 k (an increase of 26 k from case 1) at 5.5 seconds. The temperature also changed more with time compared to case 1 (Fig. 3-12b). The center temperature is 821 k at 3.5 seconds when the temperature gradient on the pellet surface is a maximum. The hoop stress on the surface reached a maximum of 172 MPa at 2.5 seconds (Fig. 3-14a) and

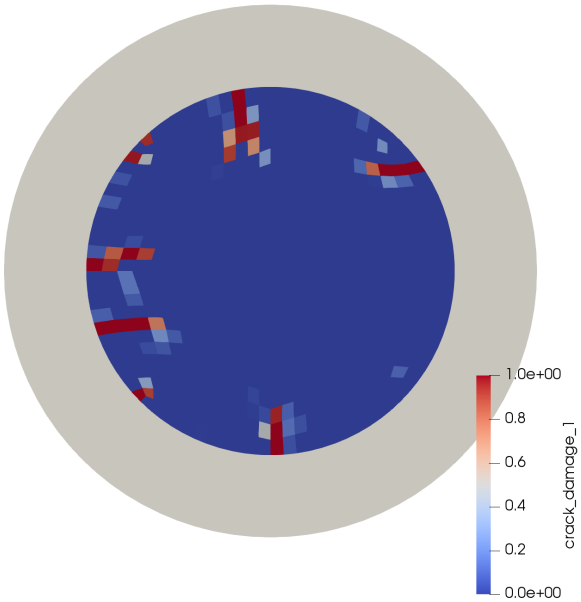

Figure 3-10: Simulated crack damage from thermal shock at 7.5 seconds (Simulated cracking damage index: 0 = undamaged; 1 = damaged).

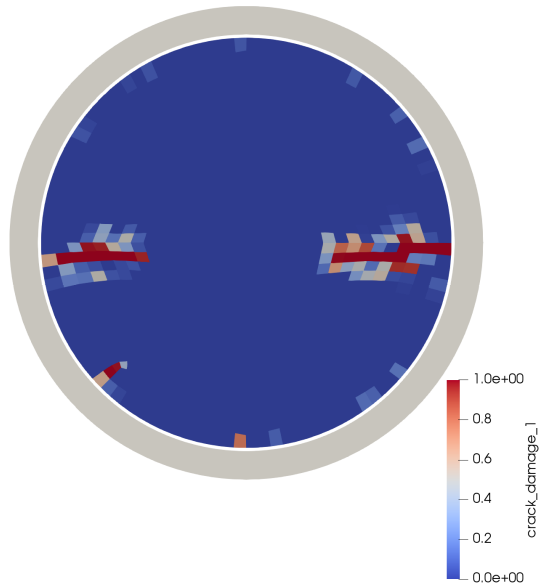

Figure 3-11: Simulated crack pattern from LWR at 8 KW/m (Cracking damage index: 0 = undamaged; 1 = damaged).

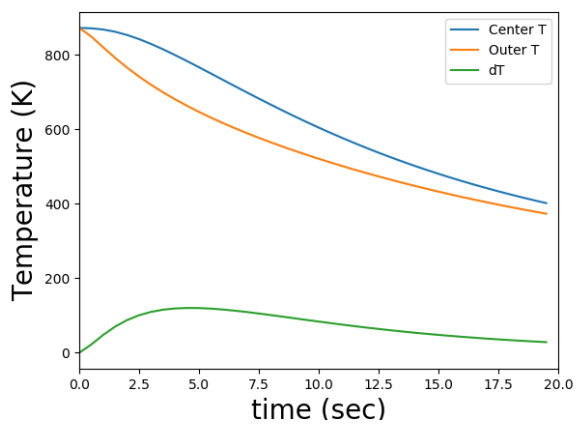

(a) Center and surface temperature change history

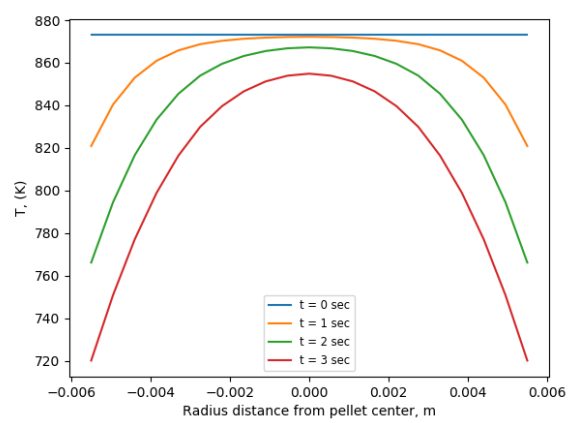

(b) Temperature profile time history.

Figure 3-12: Thermal shock result when quenched from 873 k to 228 K, with $h = 1000$ W/m^2K and $k_{gap} = 10W/mk$.

formed about 7 initial cracks at 3 seconds (Fig. 3-13). The hoop stress reached 150 MPa fracture threshold at 2 seconds and reduced on the left side due to cracking initiation at t = 3 sec (Fig. 3-14b).

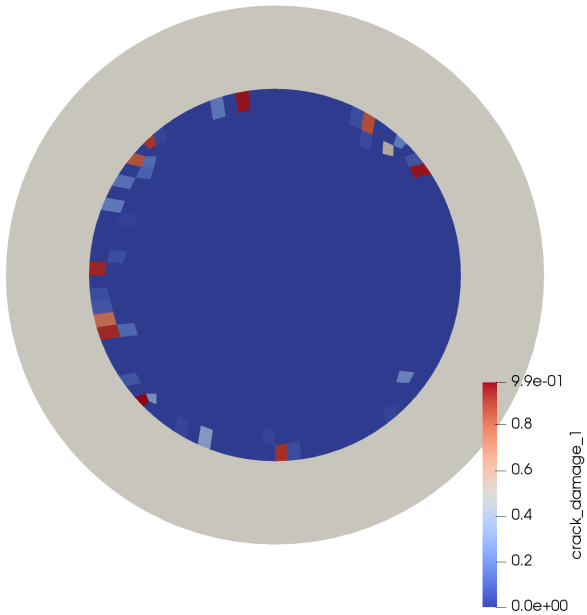

Figure 3-13: Crack initiated at 3 seconds (Cracking damage index: 0 = undamaged; 1 = damaged). Simulated result for pellet quenched from 873 k to 228 K, with $h = 1000\ W/m^2K$ and $k_{gap} = 10W/mk$.

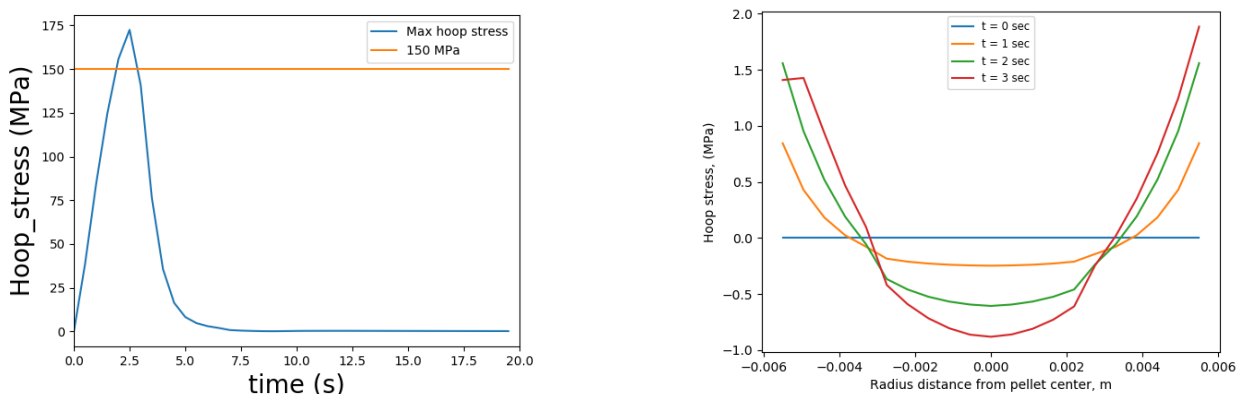

(a) Maximum hoop stress time history

(b) Hoop stress profiles time history.

Figure 3-14: Hoop stress in pellet when quenched from 873 k to 228 K, with $h = 1000$ W/m^2K and $k_{gap} = 10W/mk$.

Radial displacement on the surface is at a maximum of 32.8 μm at the beginning of the quench and shrinks down to 5.14 μm at 20 seconds (Fig. 3-15a, compared to 9.69 μm in case 1). Fig. 3-15b shows the radial displacement transitions along the horizontal centerline,

slight differences between the left end point (29 μm) and right point (28.8 μm) was due to cracking onset. Thus, cracking progresses for about 4.5 seconds then stops (Fig. 3-17). In this case, the equivalent power is 10 KW/m (Fig. 3-16). The damage pattern of that power level in an LWR is shown in Fig. 3-18.

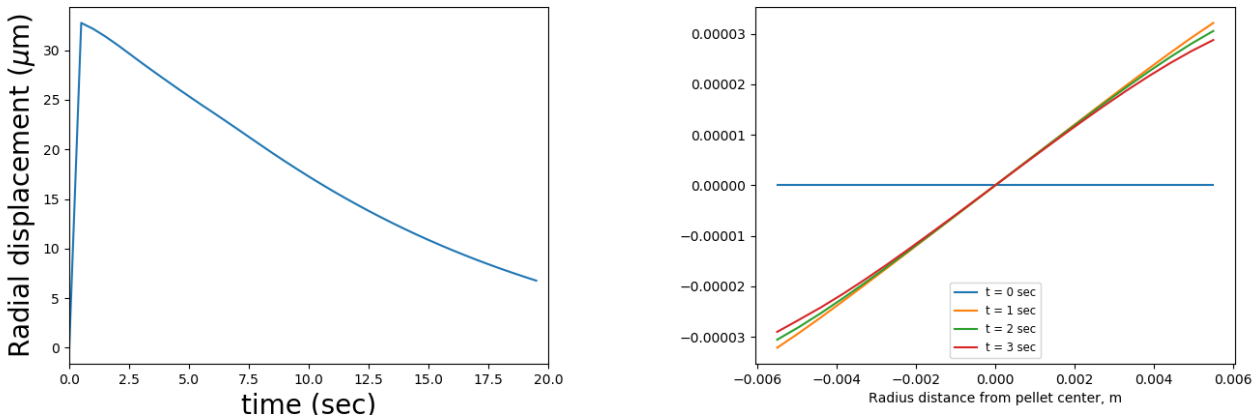

(a) Maximum radial displacement history

(b) Centerline displacement time history.

Figure 3-15: Displacement in pellet when quenched from 873 k to 228 K, with $h = 1000$ W/m^2K and $k_{gap} = 10W/mk$.

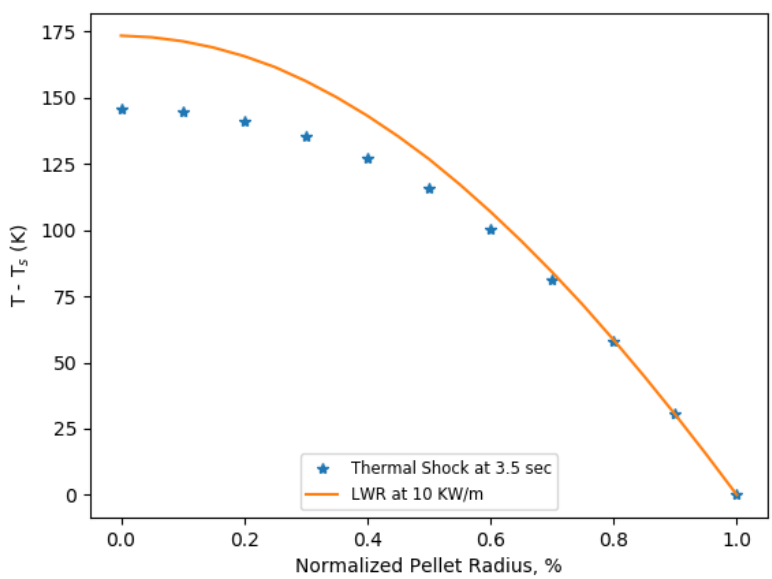

Figure 3-16: Surface temperature gradient comparison to LWR

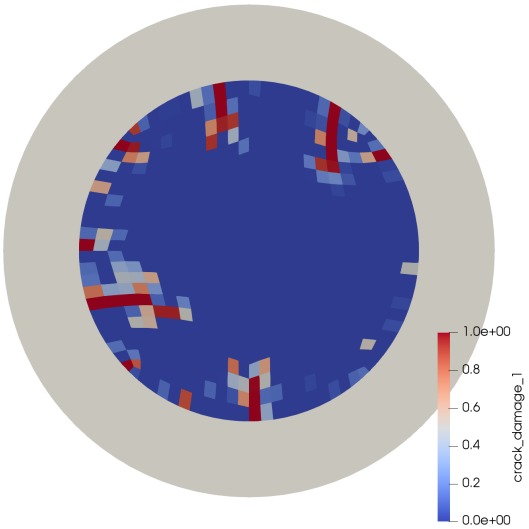

Figure 3-17: Simulated crack damage from thermal shock at 7.5 seconds (Cracking damage index: 0 = undamaged; 1 = damaged).

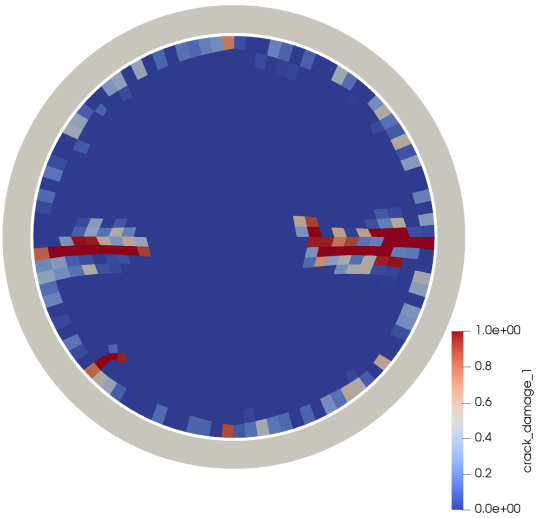

Figure 3-18: Simulated crack pattern from LWR at 10 KW/m (Cracking damage index: 0 = undamaged; 1 = damaged).

3.4.2.3 Case study 3: h = 3000 W/m^2K and k_{gap} = 10 W/mK, quenched to $-45°C$

The convective heat transfer coefficient, h, is increased to 3000 W/m^2K in the third case study. Fig. (3-19a) shows that the maximum temperature difference between the centerline and surface is 267 degrees (increasing over 100 k from case 2) at 3.5 seconds. The surface temperature drops to under 600 k in 3 seconds (720 k in case 2, Fig. 3-19b). The center temperature is 857 k at 2.0 seconds when the temperature gradient on the pellet surface is a maximum. The hoop stress on the surface reached a maximum of 211 MPa at 2.5 seconds (Fig. 3-21a) and more micro cracks initiated at 1.5 seconds (Fig. 3-20). The hoop stress reached 150 MPa fracture threshold in under 1 second and reduces on both sides due to crack initiation at t = 2 sec (Fig. 3-21b).

Radial displacement on the surface is at the maximum 32.2 μm at the beginning of the quench and shrinks down to original dimension at 16 seconds (Fig. 3-22a, compared to 5.14

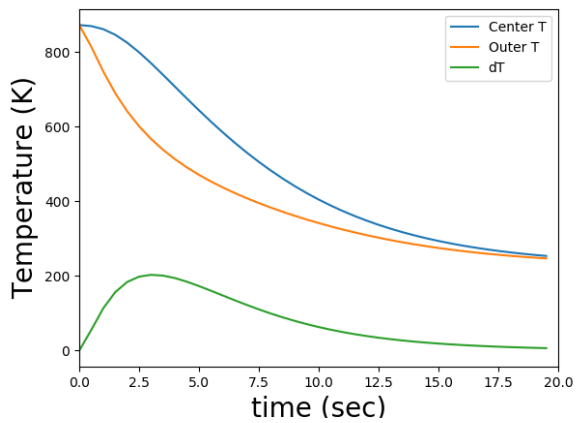

(a) Center and surface temperature change history

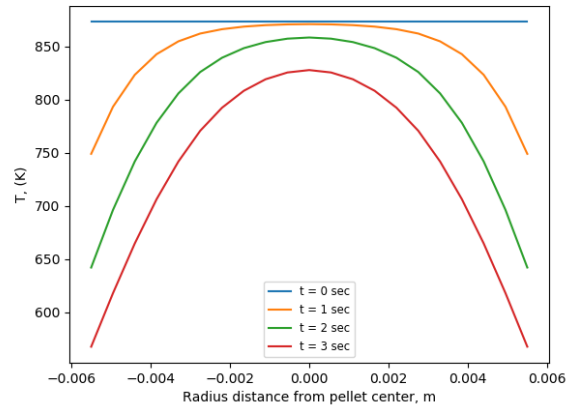

(b) Temperature profile time history.

Figure 3-19: Thermal shock result when quenched from 873 k to 228 K, with $h = 3000$ W/m^2K and $k_{gap} = 10W/mk$.

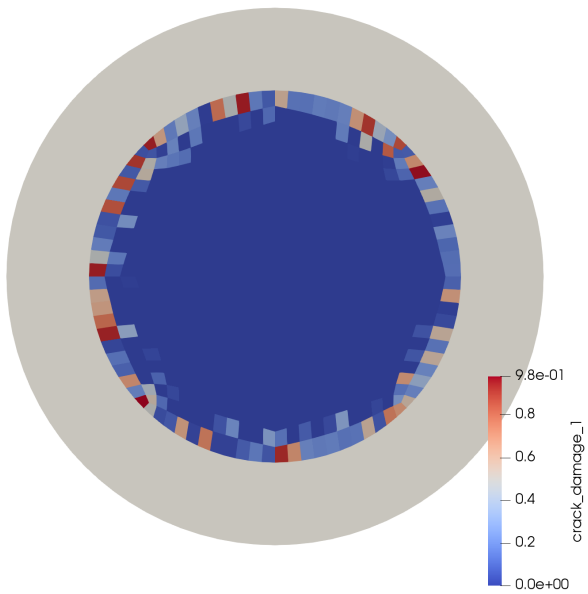

Figure 3-20: Initial cracks at 1.5 seconds (Cracking damage index: 0 = undamaged; 1 = damaged). Simulated Output for pellet quenched from 873 k to 228 K, with $h = 3000$ W/m^2K and $k_{gap} = 10W/mk$.

μm in case 2). Fig. 3-22b shows the radial displacement transitions along the horizontal centerline, slightly difference between the left end point (25.4 μm) and right point (25 μm), was due to cracking onset. Cracking progresses for about 5.5 seconds then stops (Fig. 3-24). In this case, the equivalent power is 16 KW/m (Fig. 3-23). The simulated damage pattern

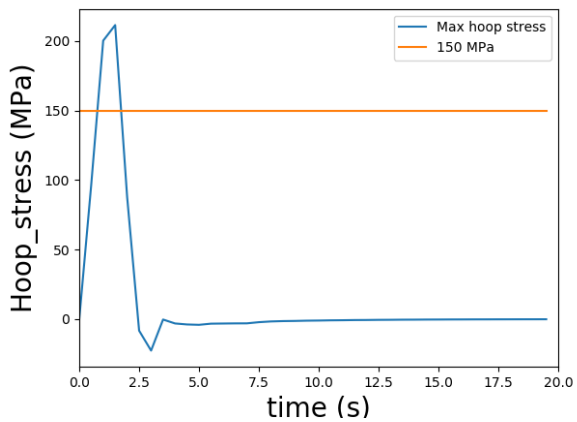

(a) Maximum hoop stress time history

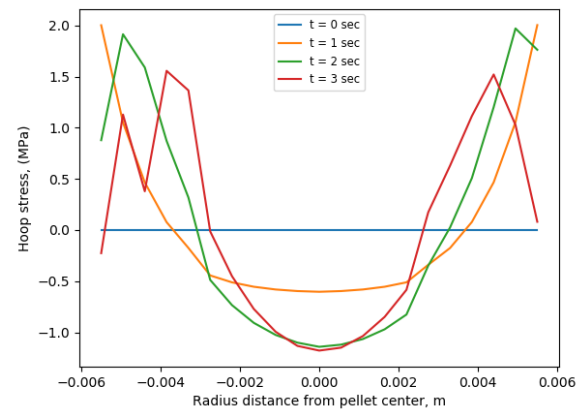

(b) Hoop stress profiles time history.

Figure 3-21: Hoop stress in pellet when quenched from 873 k to 228 K, with $h = 3000$ W/m^2K and $k_{gap} = 10W/mk$.

at that power level in an LWR is shown in Fig. 3-25.

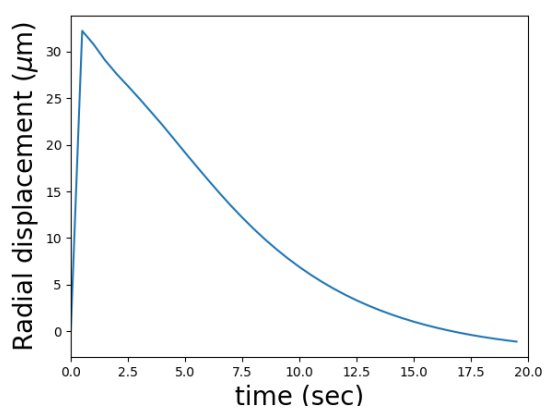

(a) Maximum radial displacement history

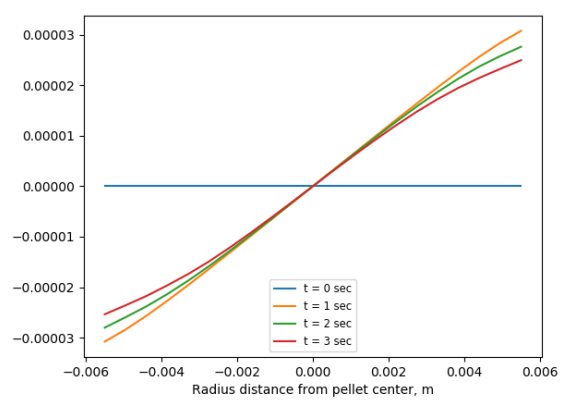

(b) Centerline displacement time history.

Figure 3-22: Displacement when quenched from 873 k to 228 K, with $h = 3000$ W/m^2K and $k_{gap} = 10W/mk$.

3.4.2.4 Case study 4: h = 3000 W/m^2K and k_{gap} = 380 W/mK, quenched to $-45°C$

The results of Case Studies 1 - 3 show that crack propagation similar to that simulated for an LWR at 8, 10 and 16 kW/m can be produced by successively increasing the heat transfer coefficient of the cold bath. In Case 4, the thermal conductivity of the gap between pellet

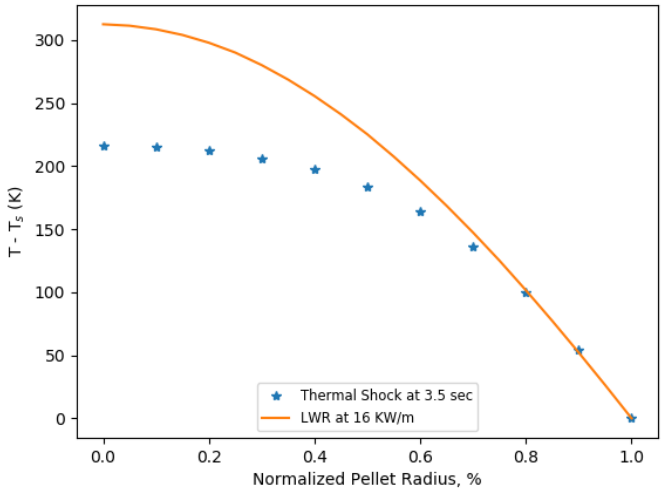

Figure 3-23: Comparison of maximum temperature gradient to LWR.

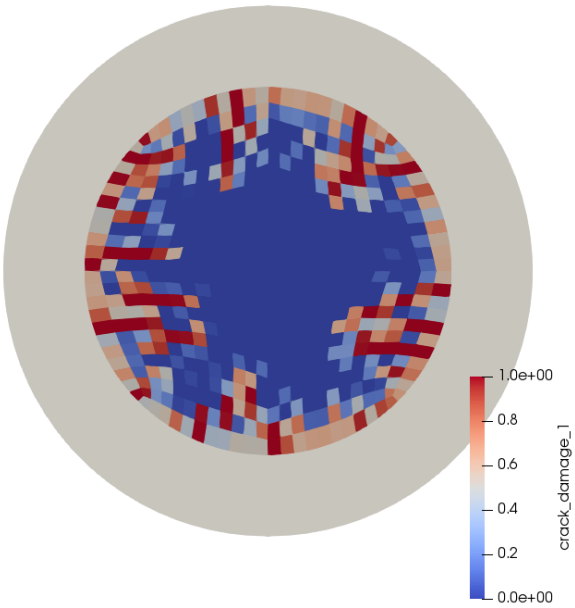

Figure 3-24: Simulated crack damage from thermal shock at 7 seconds (Cracking damage index: 0 = undamaged; 1 = damaged).

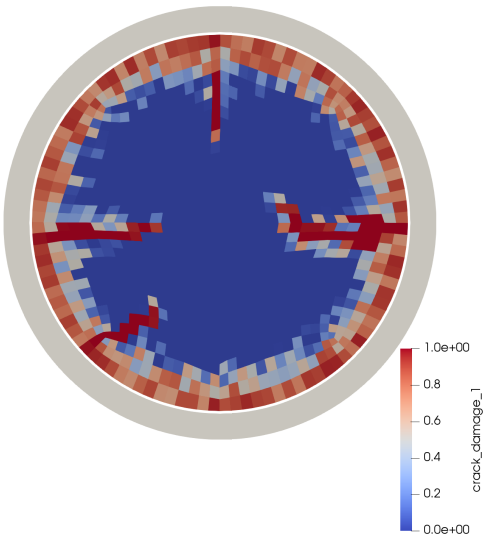

Figure 3-25: Simulated crack pattern from LWR at 16 KW/m (Cracking damage index: 0 = undamaged; 1 = damaged).

and clad is assumed to be 380 W/mK to demonstrate the cooling effect from gap conduction. Fig. (3-26a) shows that the maximum temperature difference between the pellet centerline and surface is 304 k (increasing 37 k from case 3) at 3 seconds. The surface temperature drops to under 500 k in 3 seconds (600 k in case (c), Fig. 3-26b). The center temperature is

847 k at 2.0 seconds when the temperature gradient on the pellet surface is maximum. Hoop stress on the surface reached the maximum 248 MPa at 1 second (Fig. 3-28a) and more micro cracks initiated at 1.5 seconds (Fig. 3-27). Hoop stress reached 150 MPa fracture threshold in under 1 second and reduces on the left side due to cracking initiation at t = 1 sec (Fig. 3-28b).

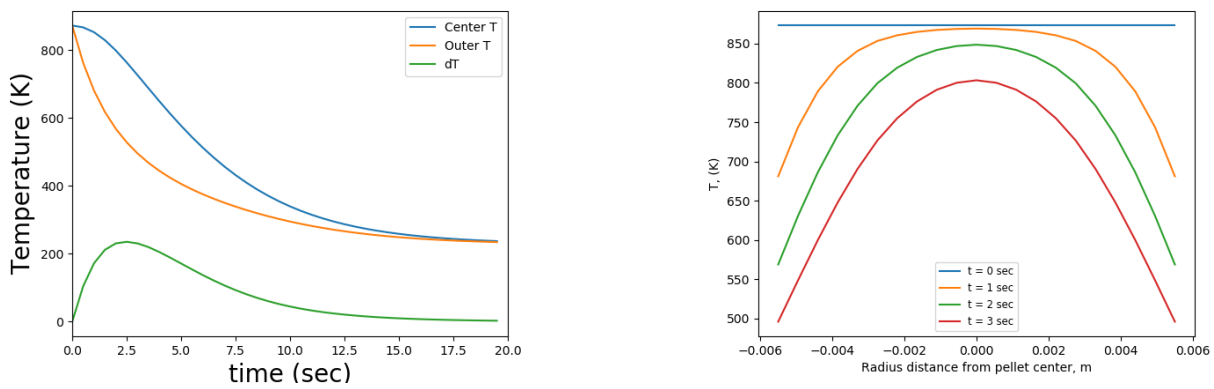

(a) Center and surface temperature change history

(b) Temperature profile time history.

Figure 3-26: Thermal shock result when quenched from 873 k to 228 K, $h = 3000\ W/m^2K$ and $k_{gap} = 380W/mk$.

Radial displacement on the surface is at the maximum 31.4 μm at the beginning of the quench and shrinks down to original dimension at 12.5 seconds (Fig. 3-29a, compared to 16 seconds in case 3). Fig. 3-29b shows the radial displacement transitions along the horizontal centerline, slight difference at 1 second between the left end point (27.8 μm) and right point (27.5 μm) is due to crack onset. Cracking progresses for about 4.5 seconds then stops (Fig. 3-30). By comparing the maximum temperature gradient at 2 seconds to an LWR, the equivalent power is 17.5 KW/m (Fig. 3-32). The damage pattern at that power level in an LWR is shown in Fig. 3-31. The simulated crack patterns for both the experiment and LWR conditions indicate more uniformly distributed micro cracks occur and large cracks may extend to half of the pellet.

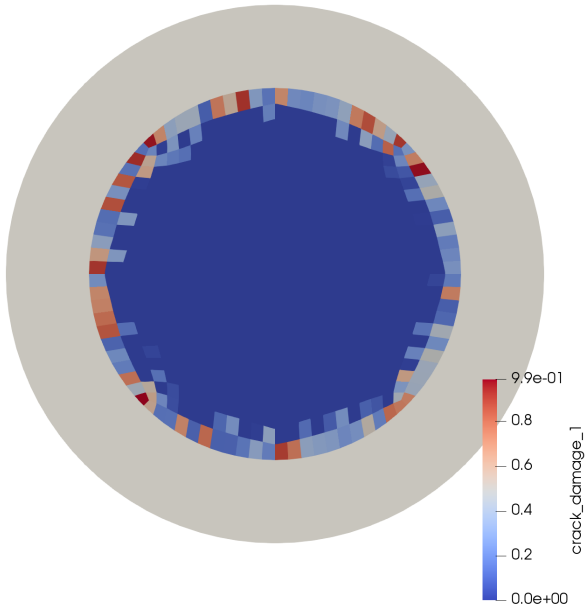

Figure 3-27: Initial cracking at 1 second (Cracking damage index: 0 = undamaged; 1 = damaged). Simulated output for pellet quenched from 873 k to 228 K, with h = 3000 W/m^2K and $k_{gap} = 380W/mk$.

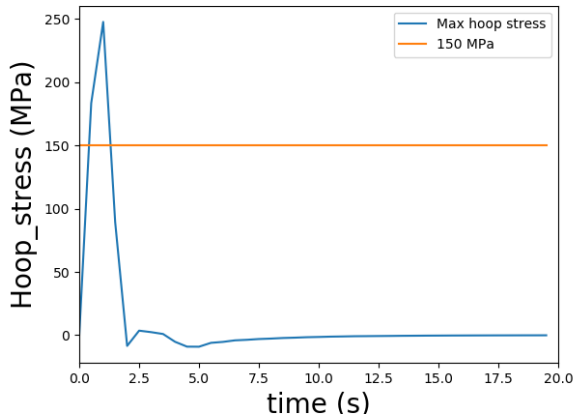

(a) Maximum hoop stress time history.

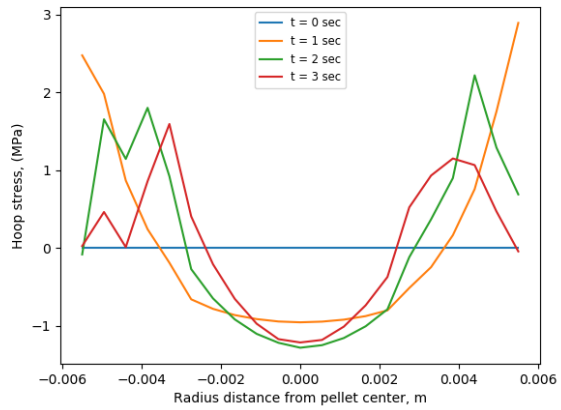

(b) Hoop stress profiles time history.

Figure 3-28: Hoop stress in pellet when quenched from 873 k to 228 K, with h = 3000 $3000W/m^2K$ and $k_{gap} = 380W/mk$.

To study the cracking propagation near full power in LWR, higher heat transfer of the cold bath is essential. It may be achieved by increasing the circulation in the cold ethylene glycol/water solution. The maximum gap thermal conductivity (assumed 100 % copper foil) yields 10 % equivalent power. From these simulation results, it may suggest improving flow

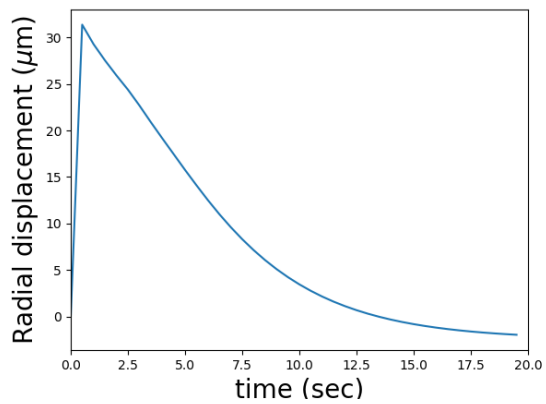

(a) Maximum radial displacement history

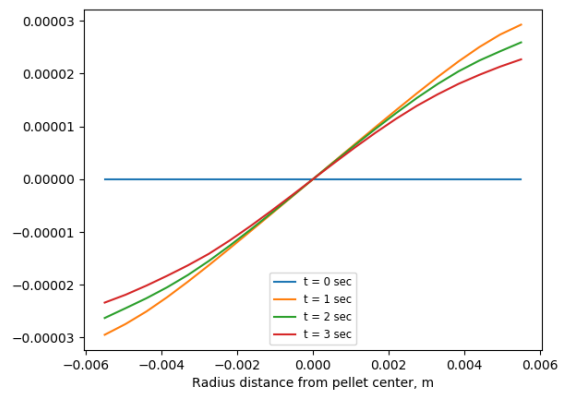

(b) Centerline displacement time history.

Figure 3-29: Displacement in pellet when quenched from 873 k to 228 K, with $h = 3000$ W/m^2K and $k_{gap} = 380W/mk$.

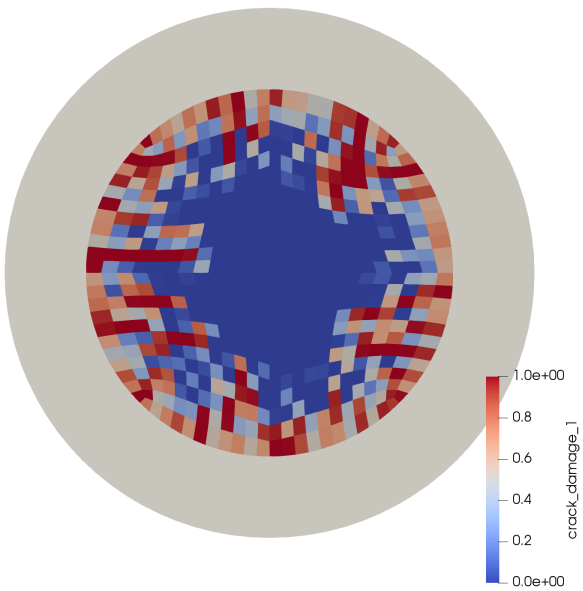

Figure 3-30: Simulated crack damage from thermal shock at 5.5 seconds (Cracking damage index: 0 = undamaged; 1 = damaged).

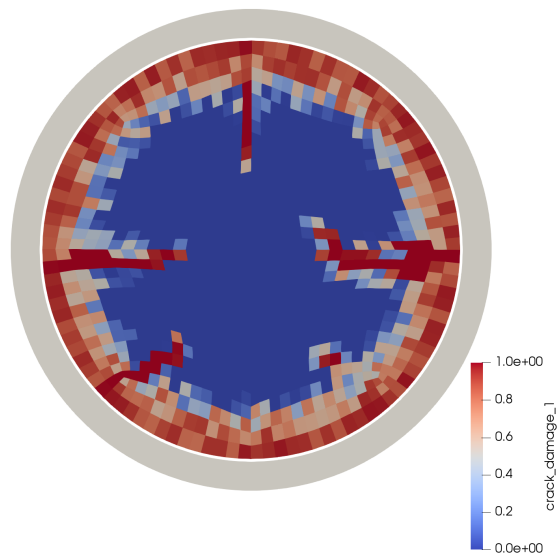

Figure 3-31: Simulated crack pattern from LWR at 17.5 KW/m (Cracking damage index: 0 = undamaged; 1 = damaged).

rate of the cold bath is more effective to achieve cracking behavior similar to higher power levels in an LWR.

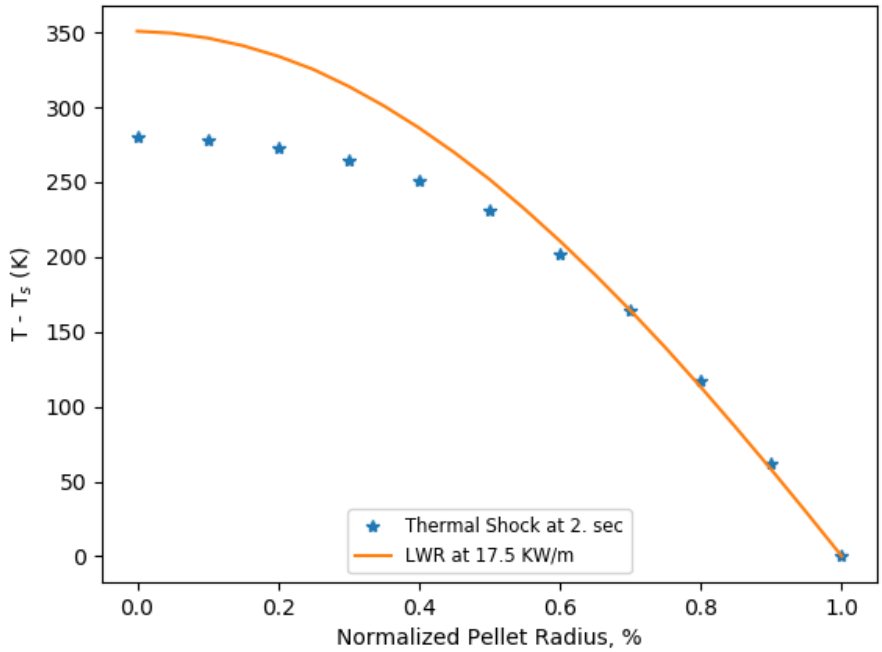

Figure 3-32: comparison of temperature gradient simulation results from thermal shock and LWR

Chapter 4

Resistive Heating

4.1 UO_2 is a Semiconductor

For out-of-pile experiments, alternative heat sources comparable to volumetric fission heat generation is required. Studies have shown that the band gap of UO_2 is between Si and GaAs. So UO_2 is a semiconductor material [Schultz, 1986] and can be used for resistance heating. According to Joule's First Law,

$$P = IV = I^2R = V^2/R$$

where P is the power generated in the material, I is the current passing through the element, V is the voltage drop and R, the electrical resistance, is the reciprocal of electrical conductance. By applying current or voltage differences, heat can be generated from converting electrical fields to thermal energy.

Bates et al. [BATES et al., 1967] summarized the electrical conductivity of near stoichiometric UO_2 in the temperature range from 300 to 3000 K (Fig. 4-1). These results show two conduction mechanisms for $UO_{2.001}$ with the transition point around 1250 K. At higher temperature, $UO_{2.001}$ behaves as an intrinsic n-type semiconductor material with activation

energy greater than 1.0 eV. At the lower temperature region, p-type extrinsic conduction is observed with the activation energy of 0.17 eV. Fig. 4-2 shows the recent data from [Ruello et al., 2005] agrees with Bates.

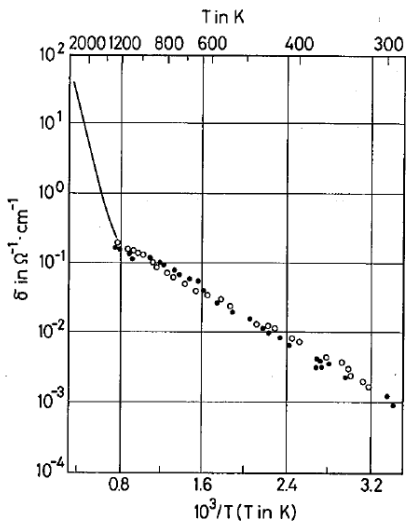

Figure 4-1: Electrical conductivity of UO_2 (for both single crystal and polycrystalline) [BATES et al., 1967].

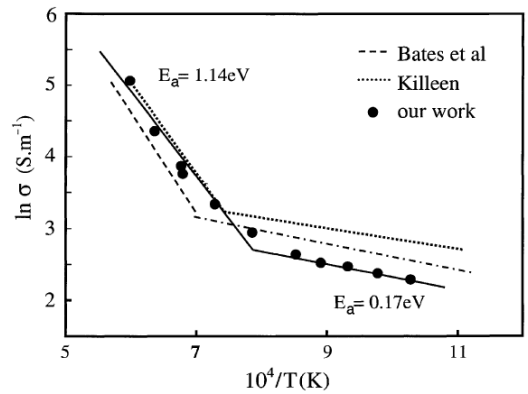

Figure 4-2: Electrical conductivity of UO_2 from [Ruello et al., 2005].)

4.1.1 Stoichiometric effect

The electrical conductivity of UO_2 strongly depends not only on temperature but also is very sensitive to stoichiometry, especially in low temperature regions. Fig. (4-3) shows the difference between the conductivity values for $UO_{2.001}$ and $UO_{1.994}$ is several orders of magnitude. As extrinsic atoms provide new energy levels between the original valence band and conduction band to the surrounding neighbors, more excited electrons or holes (with lower energy) jump into these new levels as impurity atoms (indirect jump).

UO_2 has several stable charge states: U^{3+}, U^{4+} , U^{5+} and U^{6+} [Garcia et al., 2017]. The oxygen partial pressure and temperature during UO_2 production affects U:O ratio. While

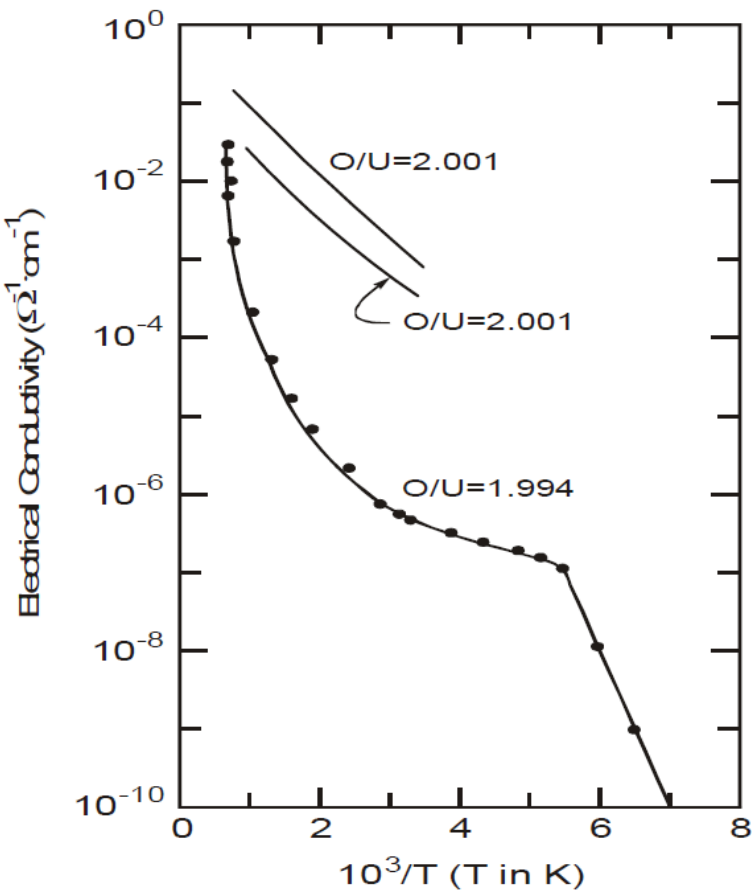

Figure 4-3: Comparison of electrical conductivity of $UO_{2\pm x}$ (single crystals) in lower temperature range [Schultz, 1986].

each interstitial oxygen atom enters a crystal unit and moves toward the equilibrium position, it pushes two surrounding lattice oxygen towards uranium. For electrical balance, this uranium changes from U^{4+} to U^{5+} [Ishii et al., 1970, Skomurski et al., 2013]. Each interstitial oxygen creates 2 UO^{5+}. Aronson *et al.*[Aronson et al., 1961] suggested that low activation energy via an ionic mechanism results in holes hopping between U^{5+} and U^{4+} cations and proposed an empirical equation of the conduction for UO_{2+x} as

$$\sigma = (3.8 \times 10^6/T)2x(1-x)exp[(-0.30 \pm 0.03eV)/kT]$$

where σ is the electrical conductivity in $(\Omega cm)^{-1}$ and x is the deviation from stoichiometry.

Increasing x gives higher conductivity. Thus to use resistive heating for a heat source in the experiments, knowledge of composition of pellets is crucial for predicting behavior. However, data may deviate due to experiment techniques, equipment, and sample quality [Ishii et al., 1970, Garcia et al., 2017].

4.1.2 Previous Research on Fuel Fracture Induced by Direct Electric Heating

Study of uranium dioxide pellet fracture and fragment relocation was conducted at Argonne National Laboratory in late 1970's [Kennedy et al., 1979]. The heat source was from direct electric heating (DEH) of the pellet itself by two independent power supplies: low-voltage, high-current (300 V and 300 A) and high-voltage, low-current (2500 V and 10 A). The voltage, current and power were adjusted to approximate the fuel temperature profiles seen in LWRs. The pellets were cooled by recirculating helium. The flow rate was manually adjusted to maintain the surface temperature within $\pm 50°C$ of the equivalent power. Thirteen thousand event of data were obtained from three test series: (1) unclad, seven pellet stack to single power cycle, (2) similar unclad stack subjected to four power cycles and (3) pellet stack in Al_2O_3 clad under different power cycles.

Important findings from the DEH studies are: initial cracks occur below reactor power 7 KW/m; little fragmentation or fragment motion was discovered even at the full power (25 KW/m); pellet center temperature change is the driving force to fragment motion, both downward and outward. Outward movement is a steady, irreversible process. The experiment was designed for empirical analysis, therefore, very limited data is available for validation purposes. However, some results and design concepts are useful for developing the proposed Joule heating experiments.

4.2 Governing equations for coupled electrical/thermal/ mechanical models

Assumptions:

- Materials are homogeneous and isotropic.
- Temperature-dependent electrical conductivity
- Thermal and electrical conduction between electrodes and fuel pellet are not included

Heat conduction equation with heat source from Joule heating:

$$\rho C_p \frac{\partial T}{\partial t} - \nabla \cdot (k \nabla T) - \dot{Q} = 0$$

where T is the temperature (K), ρ , C_p and k are density (Kg/m^3), specific heat ($J/Kg \cdot K$) and thermal conductivity ($W/m \cdot K$) of the material. $\dot{Q}$ is the heat source from Joule heating (W/m^3),

$$\dot{Q} = \mathbf{J} \cdot \mathbf{E} = J^2 \rho_e$$

where

$\mathbf{J} = \sigma \mathbf{E}$ is the current density (A/m^2),

$\mathbf{E} = \nabla \mathbf{V}$ is the electric field (Volt/m),

ρ_e is electrical resistivity (Ωm),

$\sigma = 1/\rho_e$ is the electric conductivity,

$\mathbf{V}$ is the electric potential and

Laplace's equation $\nabla^2 \mathbf{V} = 0$ applies when no unpaired electric charges exist.

Momentum conservation at static equilibrium (same as Eq. 3.3 in Thermal Shock):

$$\nabla \cdot \sigma = 0$$

$$\sigma = E\epsilon$$

$$\epsilon = \nabla_s u + \alpha \Delta T$$

$$\nabla_s u = \frac{1}{2}(\nabla u + \nabla u^T)$$

Currently there is one simple linear equation for temperature dependent electrical conductivity in MOOSE, which is only suitable for applications in a small temperature range. Therefore a better model for temperature-dependent electrical conductivity for semiconductor is needed. The basic relationship for simple intrinsic semiconductor materials is

$$\sigma = F(T) \cdot exp(-\Delta E/2kT)$$

where

σ is electrical conductivity,

$F(T)$ is a function of temperature,

T is the temperature in Kelvin,

ΔE is the energy gap between conduction band and valence band, and

k is Boltzman's constant

For most semiconductors, the energy bands are not clearly defined [Robertson et al., 1966], especially for the spinel structure of a thermistor. A thermistor is a type of semiconductor and is short for the original name: "thermally sensitive resistor". They are used for precision temperature measurement with electrical resistance.

The Steinhart-Hart Equation (named after John S. Steinhart and Stanley R. Hart in 1968, [Steinhart and Hart, 1968]) describes the relationship of the resistance of a semiconductor to temperature.

$$\frac{1}{T} = A + B\ln(R) + C[\ln(R)]^3$$

where

T is the temperature in Kelvin

R is the electrical resistance in ohms

A, B and C are Steinhart-Hart coefficients

Originally the squared term was included, but it is left out for the coefficient is negligible compared to other coefficients. It has been well accepted by the thermistor industry; companies publish their own coefficient constants A, B and C for individual products. The linear version (without $C[\ln(R)^3]$ term) of the Steinhart-Hart equation was implemented and merged into MOOSE [1] since the energy gaps of UO_2 in both high and low temperature range are defined. This model can be easily expanded to a full version (including $C[\ln(R)^3]$ term) as the resistance of a semiconductor at a given temperature is derived [2].

4.3 Experiments

4.3.1 Proposed Studies

Fuel fracture experiment induced by resistive heating [3] is planned to use a thermal camera to record temperature change and fracture propagation across the top of the pellet. Electrodes will be placed on the side so they do not impede the top view, unlike the DEH experiment

[1] SemiconductorLinearConductivity
[2] `https://en.wikipedia.org/wiki/Steinhart-Hart_equation`
[3] Proposed by Dr. Knight and Dr. Besmann at University of South Carolina

([Kennedy et al., 1979]) in which electrodes were placed at the top and bottom of the pellet stack.

4.3.2 Schematics

Three configurations were simulated and are discussed here (Fig. 4-4a - 4-4c): (a) two point electrodes on opposite sides of the pellet; (b) four point electrodes placed at 90° intervals around the sides of the pellet, and (c) two arc electrodes, spanning 1/8 of the pellet circumference, on opposite sides of the pellet. To observe crack initiation and propagation, the design is focused on the least interference to the thermal expansion and fracture. Point electrodes were first investigated because of small contact area. However the temperature profile is not symmetric as it is in LWR normal operation condition. Another pair of electrodes was added to the vertical centerline. While the results are closer to what is seen in LWR conditions, technical difficulties were introduced, such as maintaining contact between pellet and electrodes without introducing any extra force. Final design included two wider arc electrodes. In addition to the three experimental configurations, the early DEH experiments were also simulated (Fig. 4-4d).

4.4 Results and Discussion

4.4.1 Two point electrodes on the sides

• Applied constant voltage of 133 V at an initial temperature of 400 K and a convective heat transfer coefficient = 10000 W/m^2K

Applied constant voltage was first tested for it is easier to setup. As seen in Fig. 4-5, the highest temperature is about 590 K near the two electrodes and the hotter zone is in the shape of a lens with two hot spots near the electrodes. Since the thermal conductivity at the

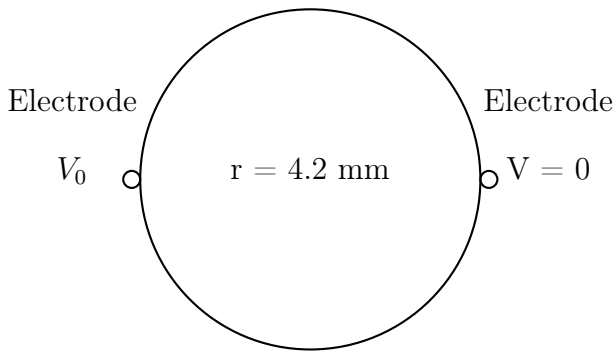

(a) Two point electrodes on the sides

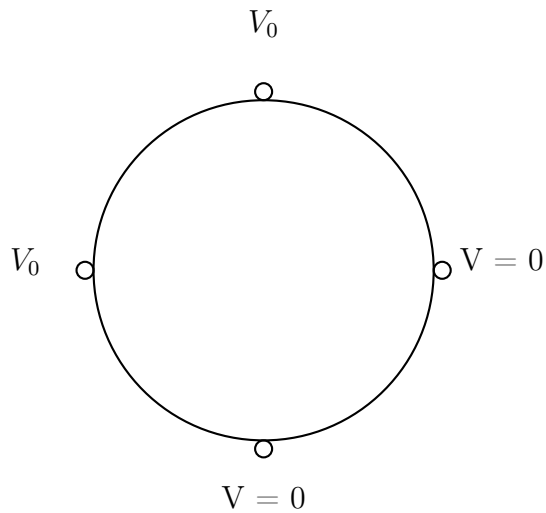

(b) Four point electrodes on the sides

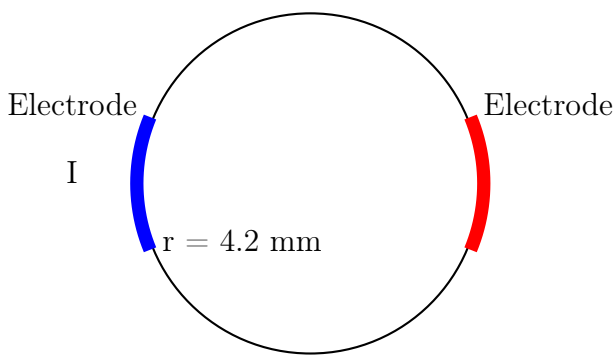

(c) Two side electrodes on the sides

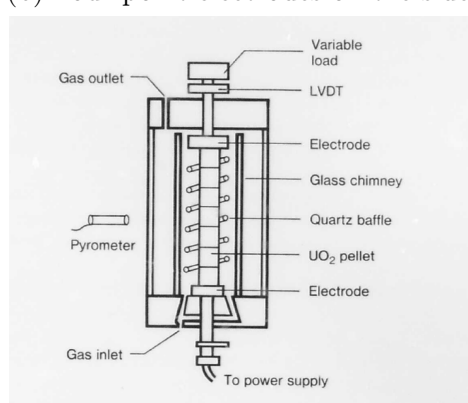

(d) Experiment setting from Argonne DEH experiment, [Kennedy et al., 1979]

Figure 4-4: Configurations of electrodes and fuel pellets

center of the pellet is lower at higher temperature and the heat transfer to the surrounding atmosphere is higher (no heat source along the vertical centerline), the maximum heat flux is near the electrode. In the outer annulus, the lowest heat flux is in the hotter lens shape zone. The electrical field distribution and current density are also exhibited in Fig. 4-5.

4.4.2 Four point electrodes

• Applied constant voltage of 114 V at an initial temperature of 400 K and a convective heat transfer coefficient = 10000 W/m^2K.

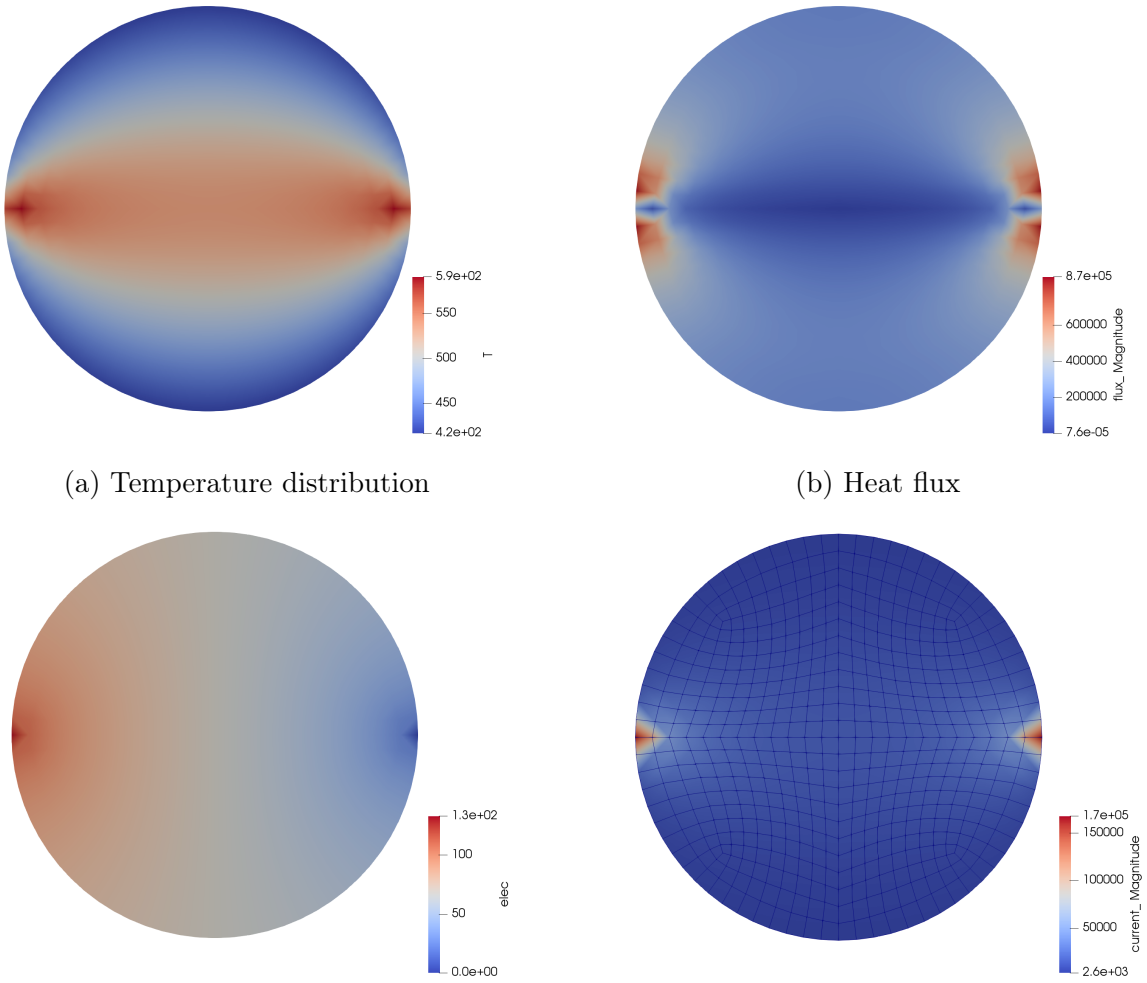

(a) Temperature distribution

(b) Heat flux

(c) Electrical field

(d) Current Density

Figure 4-5: Simulation output of 2 electrodes

As the lens shape temperature distribution does not describe the temperature profile in an LWR from a volumetric heating source perspective, another pair of point electrodes are added for a better match. Voltage is applied at two locations (90° apart) on the pellet side (Fig. 4-6) and the current flows through the pellet to the opposite end. As electrical and thermal physics are tightly coupled, heat removal on the pellet surface causes some electrical current to flow along the surface (northwest quadrant), converge at 45° and pass through the pellet center. Temperature distribution is in a 4-point starfish-like (convex) shape. More heat flux moves outward on the surface. Lower thermal conductivity at the center leads to

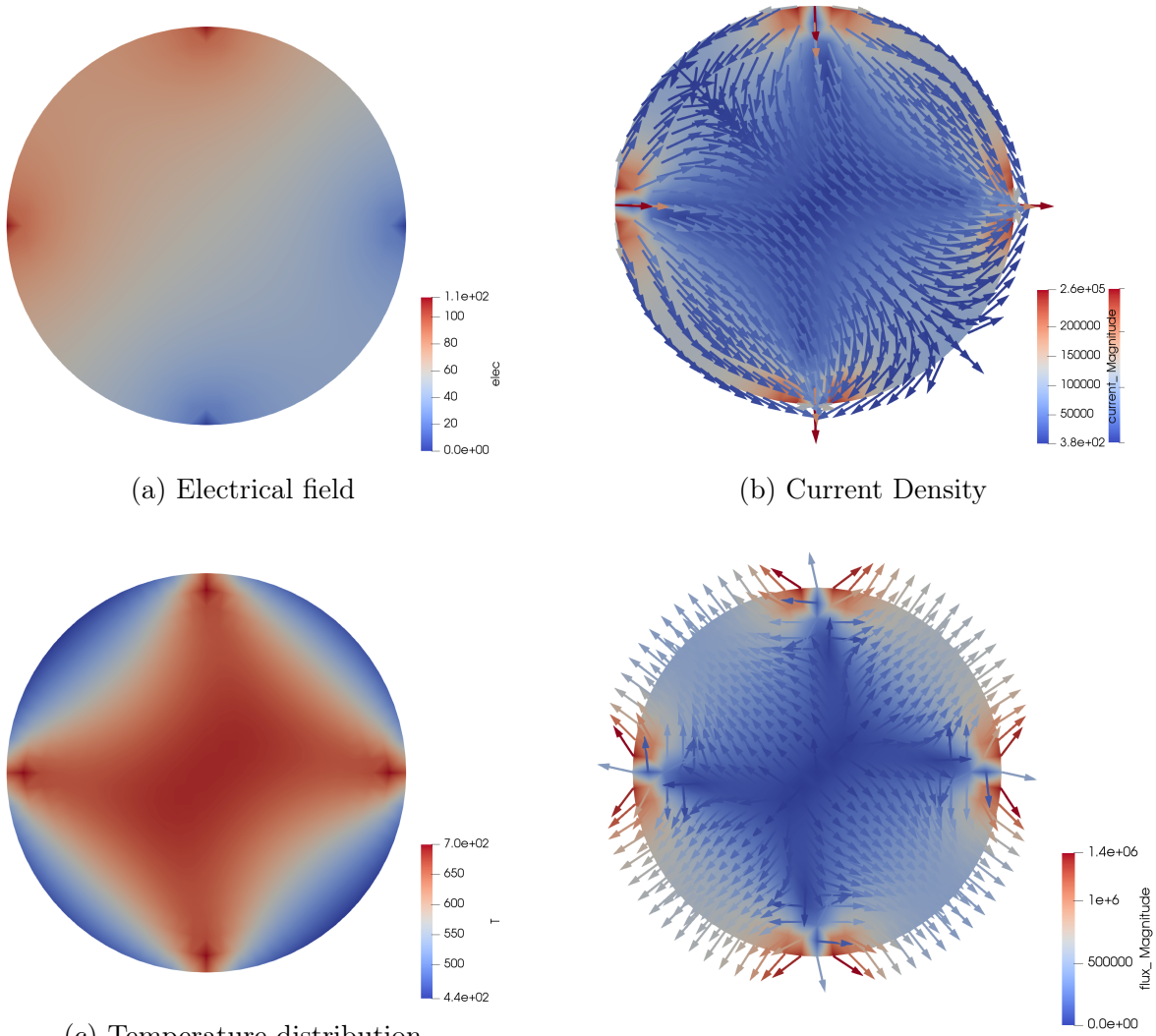

(a) Electrical field

(b) Current Density

(c) Temperature distribution

(d) Heat flux

Figure 4-6: Simulation output for 4 electrodes

slower movement in the center. An extra pair of electrodes produces a more symmetrical temperature distribution, yet more moving parts in the physical setup leads to technical difficulty.

4.4.3 Two arc electrodes on the sides

To employ wider electrodes to enhance the temperature profile shape closer to LWR conditions (concave) and not restrain thermal expansion and cracking, arc electrodes were placed over 1/8 of circumference of the pellet.

4.4.3.1 h = 10000 W/m^2K

4.4.3.1.1 Constant Voltage - Initial temperature = 500 K and applied voltage = 80 Volt

Fig. 4-7 shows the time histories of the center and surface temperatures and temperature distribution. Contrary to thermal shock experiments (high to low), the pellet temperature increases from a Joule heating heat source. With a constant voltage, pellet temperatures increases at a very fast rate. The flat temperature profile of the inner region reflects the coupling effect of electrical and thermal physics: Fig. 4-8a and 4-8c show the electrical field and current density distribution. The temperature profile is an oval shape, convex along the horizontal centerline and concave on the vertical centerline (Fig. 4-8b). Two large fractures near the electrodes and a fair amount of minor cracks on the surface between two electrodes (Fig. 4-8d) are observed. Due to the concern of continuous cracking during a temperature excursion, the experimenters are switching toward applying constant current.

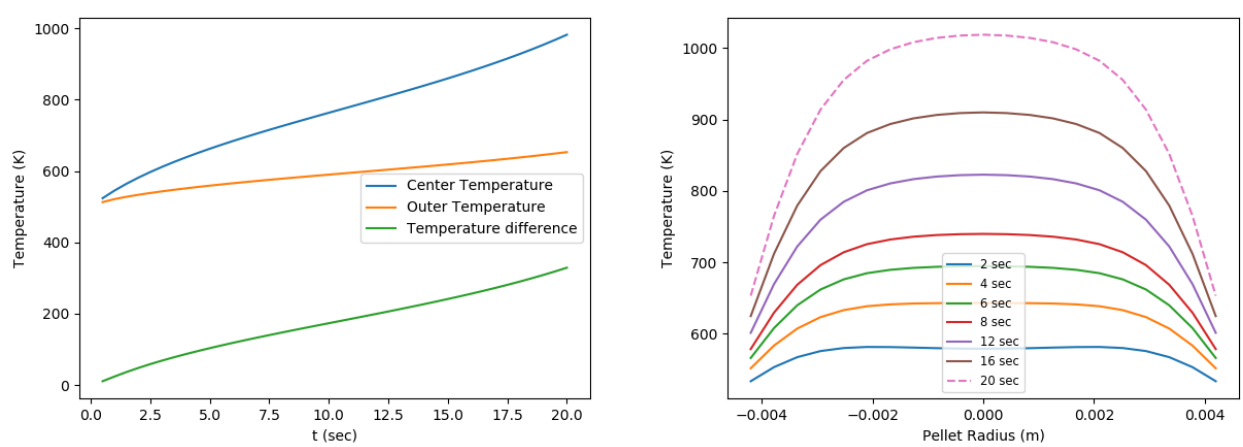

(a) Temperature profile time history

(b) Temperature profiles changes

Figure 4-7: Thermal results for simulation at constant voltage (80 V) and initial pellet temperature 500 K.

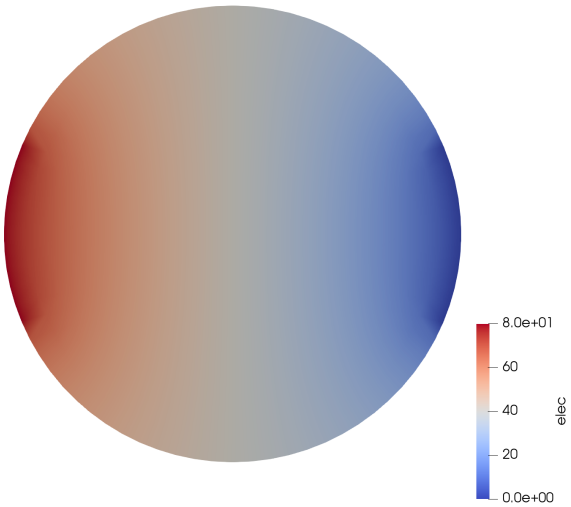

(a) Electrical Field

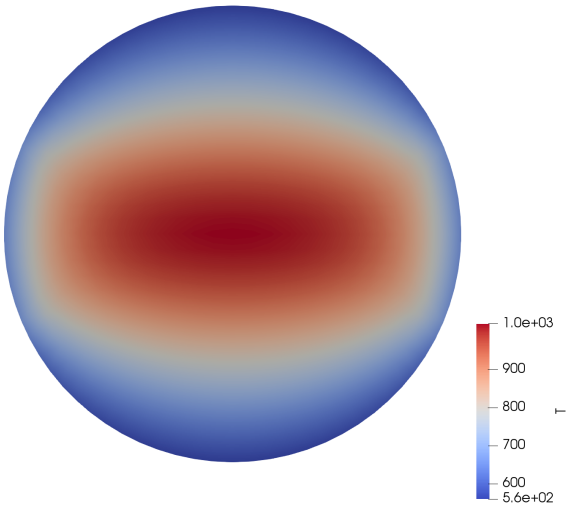

(b) Temperature profile

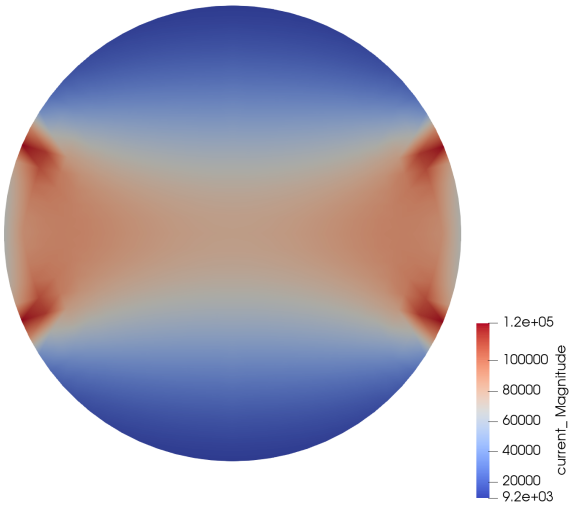

(c) Current Density

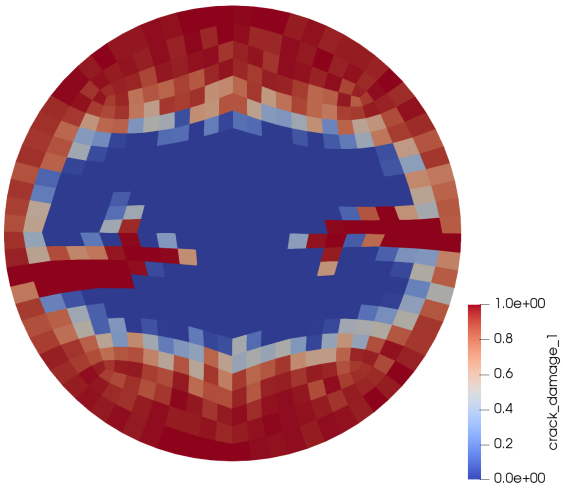

(d) Crack pattern

Figure 4-8: Simulated output of applied constant voltage from two arc electrodes

4.4.3.1.2 Constant Current

The advantage of applying constant current is the current will reach equilibrium and the temperature profile will approach a steady state.

4.4.3.1.3 Initial temperature = 673 K and applied current = 4.6 Amps

When a constant current of 4.6 amperes is applied to a pellet with starting temperature 673 K, the center temperature increases to 903 K and the surface temperature to 745 K. Both center temperature and surface temperature reach steady state and the difference is about 158 degrees at 10 seconds (Fig. 4-9). There are two peaks in the temperature profile at the beginning of the experiment (Fig. 4-10c). This is because of the high heat removal rate on the surface, which leads to lower electrical conductivity/high resistivity. Thus, more resistive heat is generated near the surface which leads to higher temperature (peaks on the both ends). In this case, these two peaks move towards the center region with time and merge into one. On the horizontal centerline between the two electrodes, the temperature distribution is a convex shape. On the other hand, without heat source along the vertical centerline, the temperature profile is concave.

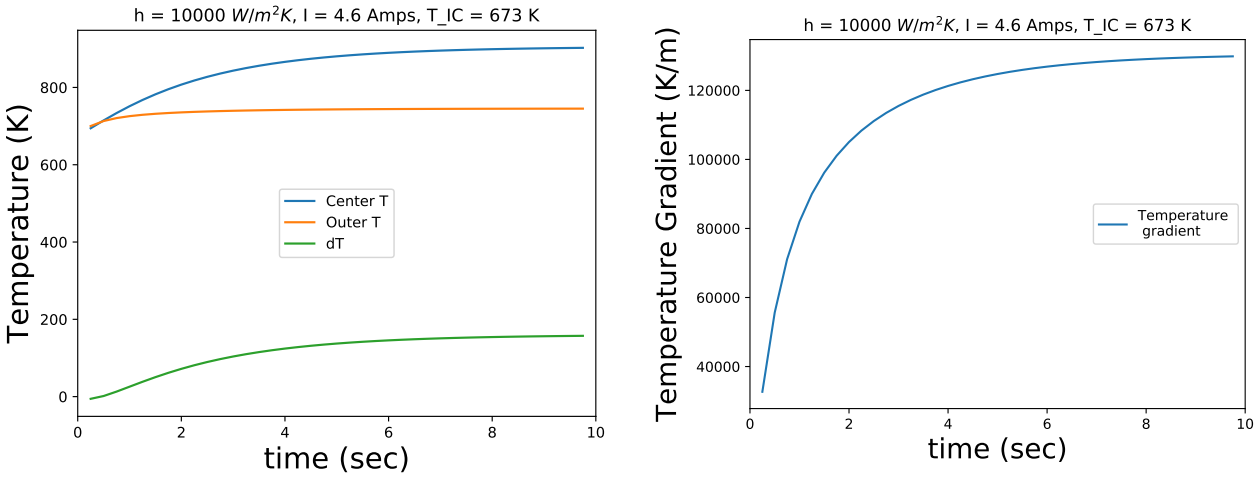

(a) Temperatures

(b) Temperature gradient

Figure 4-9: Horizontal centerline temperature time history

Fig. 4-11 shows the distributions of the electrical field, current density, temperature profile and heat flux at 10 seconds. The red hot temperature zone is an oval shape; closer to symmetric as in an LWR. Similar to the thermal shock experiment, heat flux is lower at the center hot zone and higher near the electrodes, opposite of the temperature profile. Heat

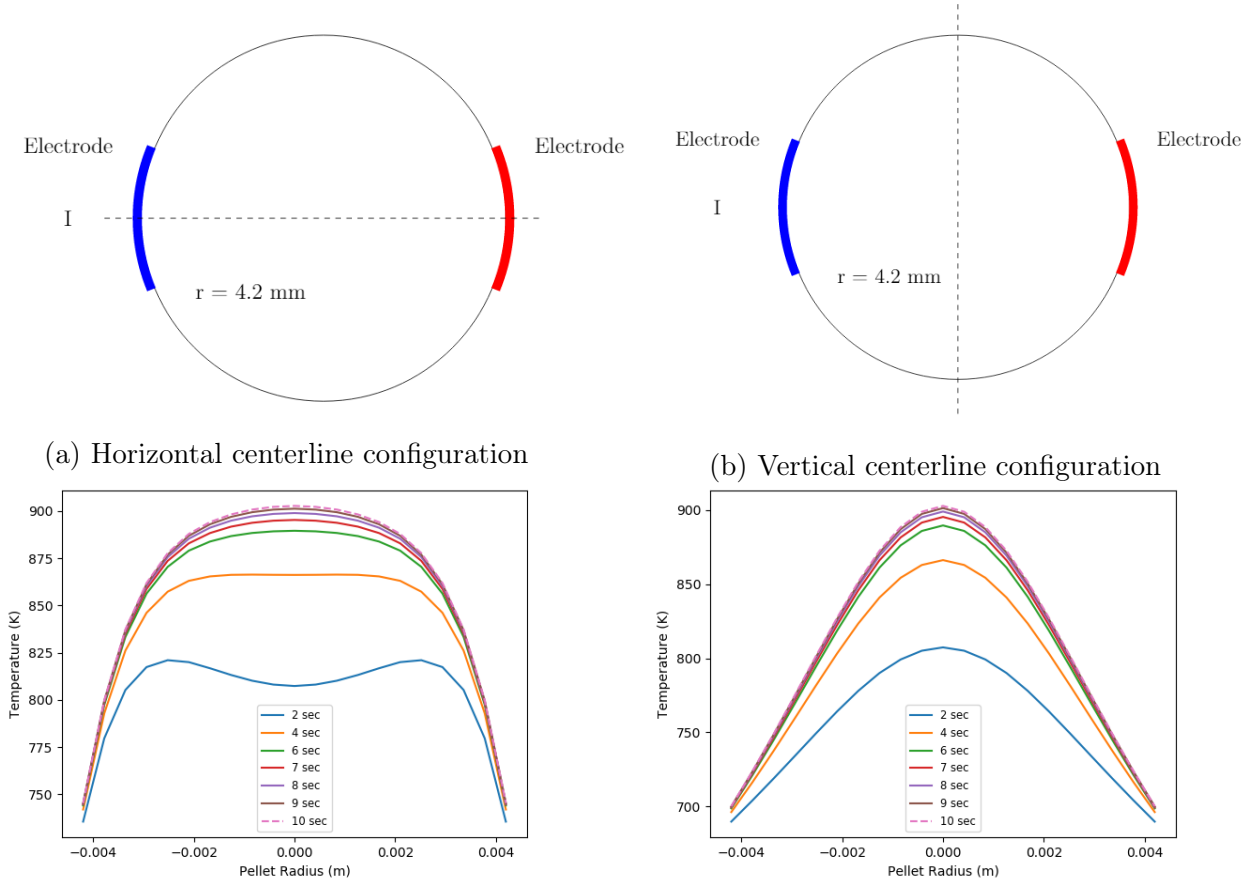

(a) Horizontal centerline configuration

(b) Vertical centerline configuration

(c) Horizontal centerline

(d) Vertical centerline

Figure 4-10: Thermal results for simulation at constant current (4.61 amp) and initial pellet temperature 673 K.

generation is highest at the edges of the arc electrodes and slightly less significant along the surface of the pellet under the electrodes. The pellet displacement is 26.6 μm. Two initial cracks occur at 1.5 seconds near the electrodes and progress toward the center and stop when they reach the compressed region at 7.5 seconds (Fig. 4-12). Comparing the temperature gradient on the surface in a normalized radius, the cracking pattern is equivalent to an LWR at 16.5 KW/m power level (Fig. 4-13).

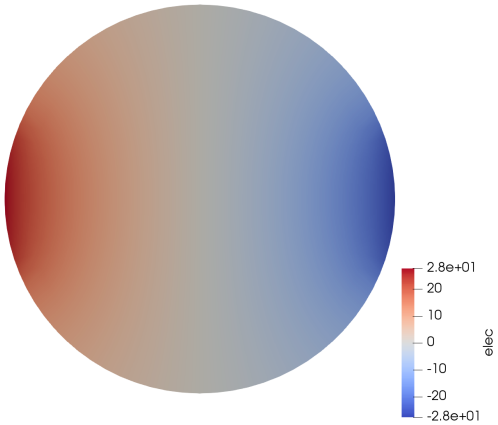

(a) Electrical Field

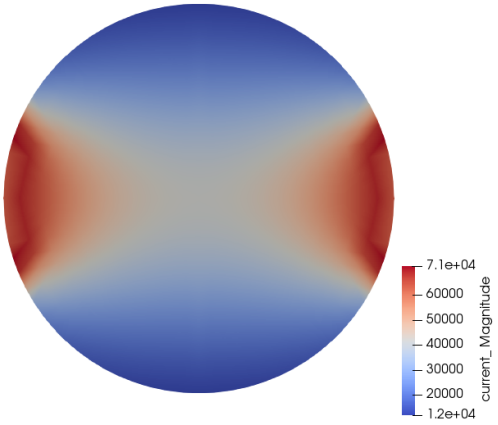

(b) Current Density

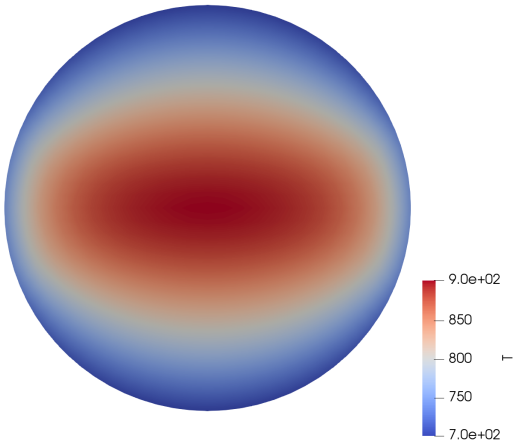

(c) Temperature profile

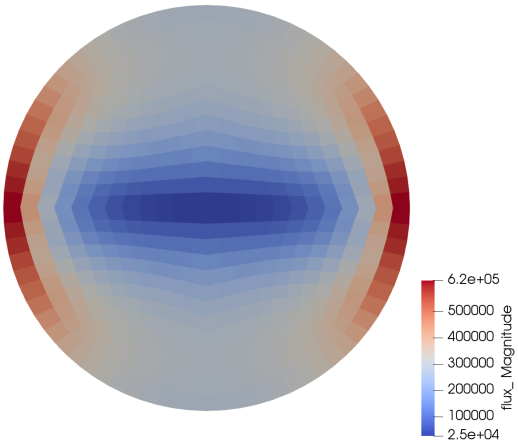

(d) Heat flux

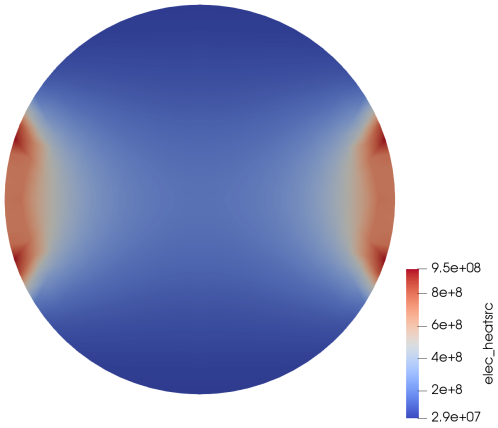

(e) Heat generated from resistive heating

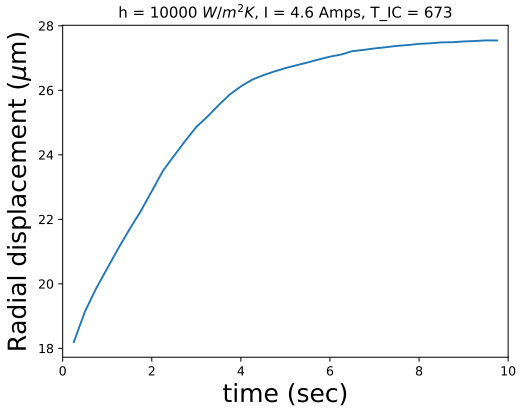

(f) Displacement along horizontal centerline

Figure 4-11: Simulated output of applied constant current from two arc electrodes, T_{init} = 673 K and I = 4.6 Amps

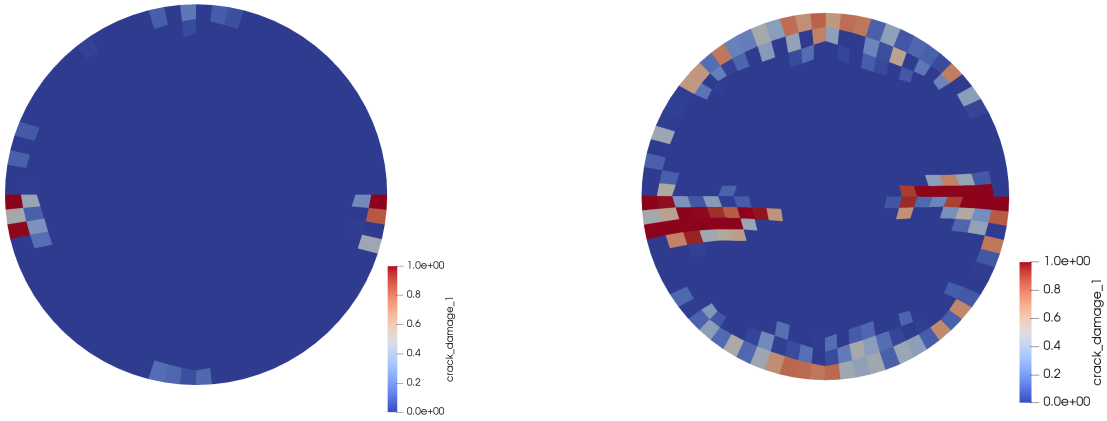

(a) (b)

Figure 4-12: (a) Initial cracking at 1.5 seconds and (b) propagation stops at 7.5 seconds, T_{init} = 673 K and I = 4.6 Amps

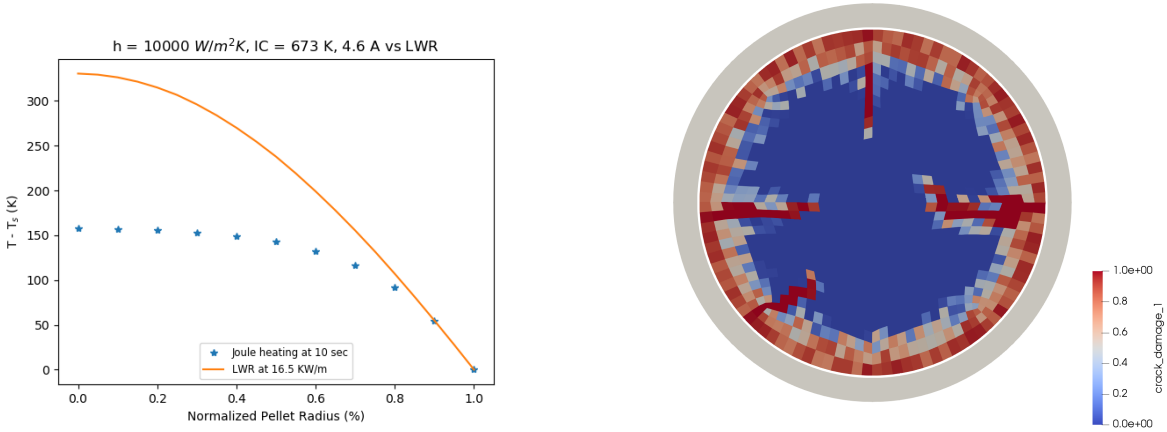

(a) (b)

Figure 4-13: (a) Comparison of temperature gradient with LWR, (b) Cracking pattern of LWR at 16.5 KW/m power level.

4.4.3.1.4 Initial temperature = 573 K and applied current = 2.6 Amps

When a constant current of 2.6 amperes is applied to a pellet with starting temperature 573 K, the center temperature increases to 652 K and the surface temperature decreases to 557 K and the displacement is 16.4 μm. Figs. 4-14 and 4-15 show a lower temperature profile and a smaller crack, compared to the previous case. The equivalent LWR power level is 10.75 KW/m.

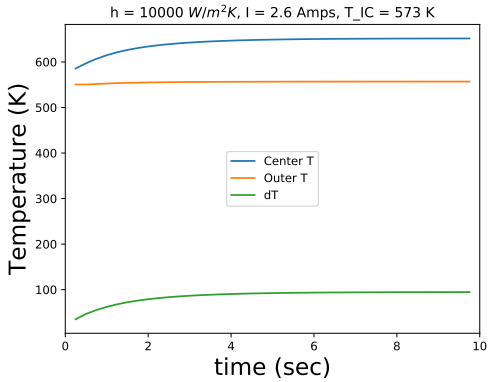

(a) Temperatures

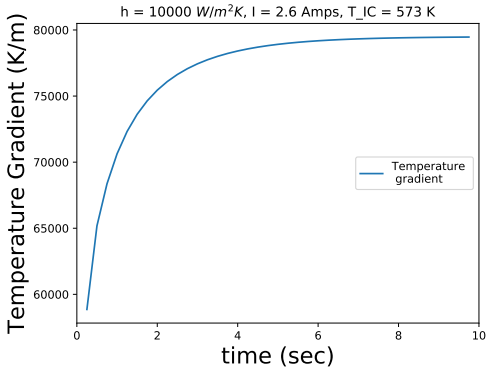

(b) Temperature gradient

Figure 4-14: Horizontal centerline temperature time history.

4.4.3.1.5 Initial temperature = 873 K and applied current = 2.6 Amps

When a constant current of 2.6 amperes is applied to a pellet with starting temperature 873 K, the center temperature increases to 907 K and the surface temperature decreases to 628 K and reaching steady state at 822 K (Fig. 4-16). This behaviour is opposite the previous two cases but similar to that in the thermal shock experiments . The electrical conductivity at this temperature is higher, therefore lower heat energy has been generated than heat removal. There is a high density of micro cracks around the perimeter appearing at the very beginning (Fig. 4-17). A few cracks grow into the pellet center about one half of radius (stopping at 3.5 seconds), which is similar to an LWR at full power, 25 KW/m (Fig. 4-18).

4.4.3.2 h = 500 W/m^2K

4.4.3.2.1 Initial temperature = 573 K and current = 7.9 Amps

With lower convective heat transfer around the surface, heat inside the pellet is built up faster. The center temperature is over 1600 K; the surface temperature near the electrodes is 1524 K as more heat is generated around the region. The temperature is 1274 K along the

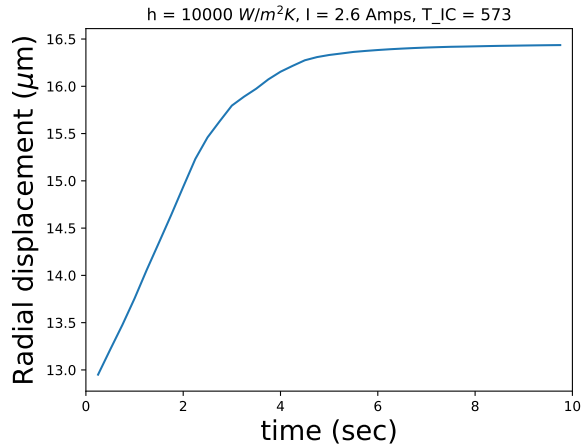

(a) Displacement

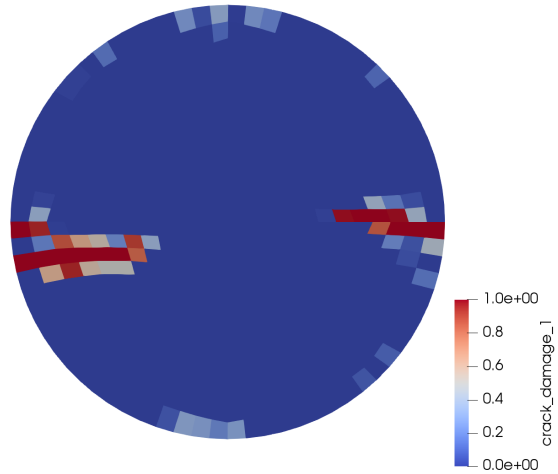

(b) Crack pattern

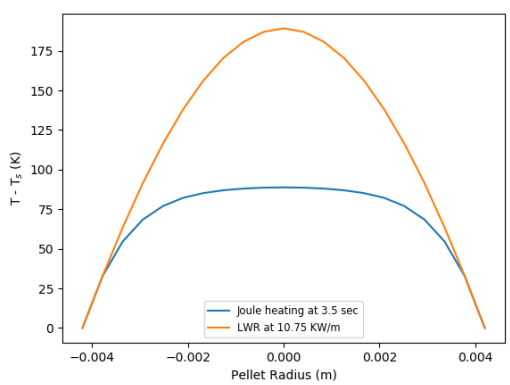

(c) Comparison of temperature gradient with LWR

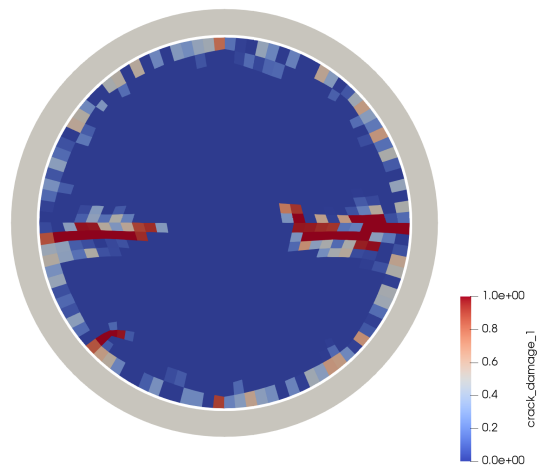

(d) Cracking pattern of LWR at 10.75 KW/m power level

Figure 4-15: Simulated output of applied constant current from two arc electrodes, T_{init} = 573 K and I = 2.6 Amps

vertical centerline (Fig. 4-19). The temperature difference between center and surface along the vertical centerline is over 200 degrees before 3 seconds and almost 400 degrees when it reaches steady state (after 35 seconds). However on the horizontal centerline, during the first 8 seconds the center temperature is lower than the surface temperature and the temperature difference is only 145 degrees (Fig. 4-20).

In addition to two small cracks near the electrodes, several cracks initiated on the top and

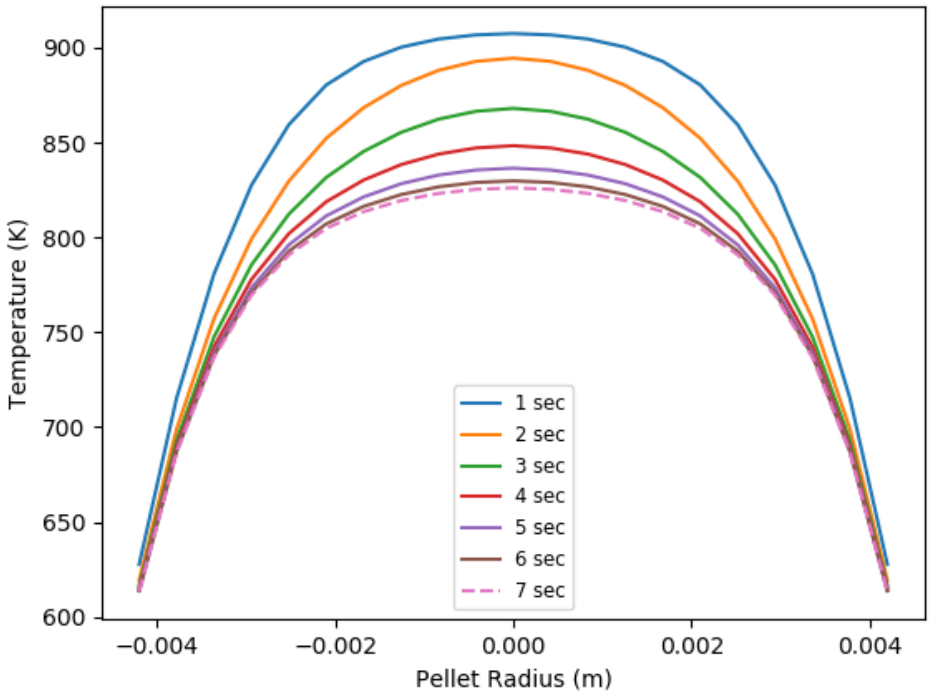

Figure 4-16: Thermal results for simulation at constant current (4.6 amp) and initial pellet temperature 873 K.

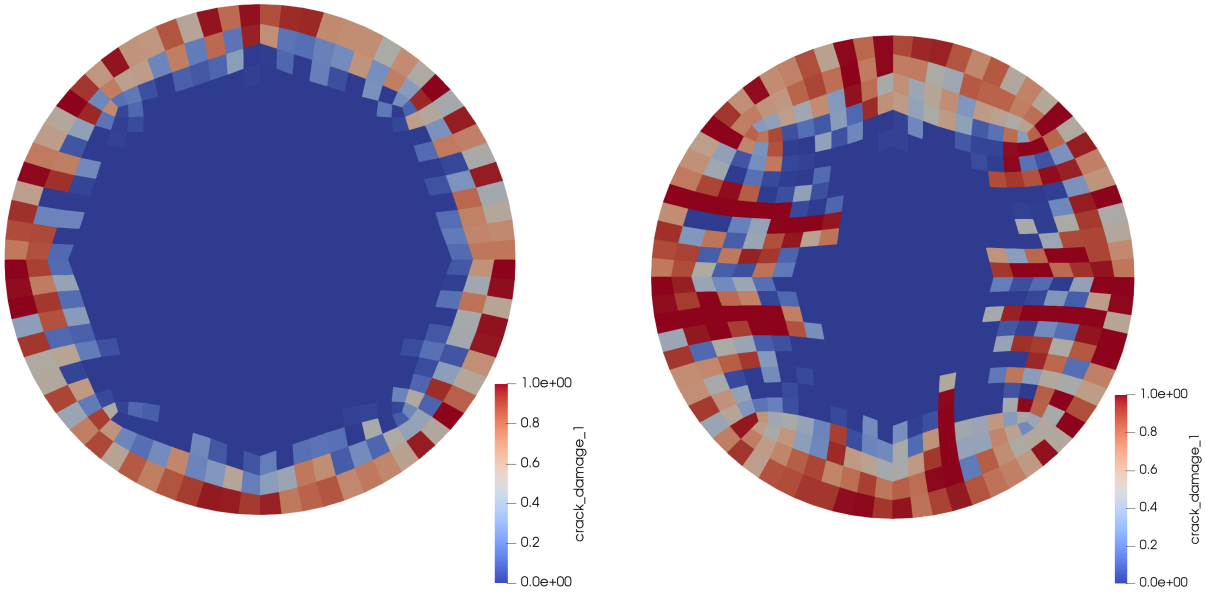

(a) Initial cracking at 0.5 seconds

(b) Cracking pattern at 3.5 seconds

Figure 4-17: Simulated cracking pattern of Joule heating, initial temperature = 873 K

bottom (Fig. 4-21). Cracks on the sides progress and more cracks form between electrodes up to 12.25 seconds. The equivalent LWR power level is 18 KW/m comparing the tempera-

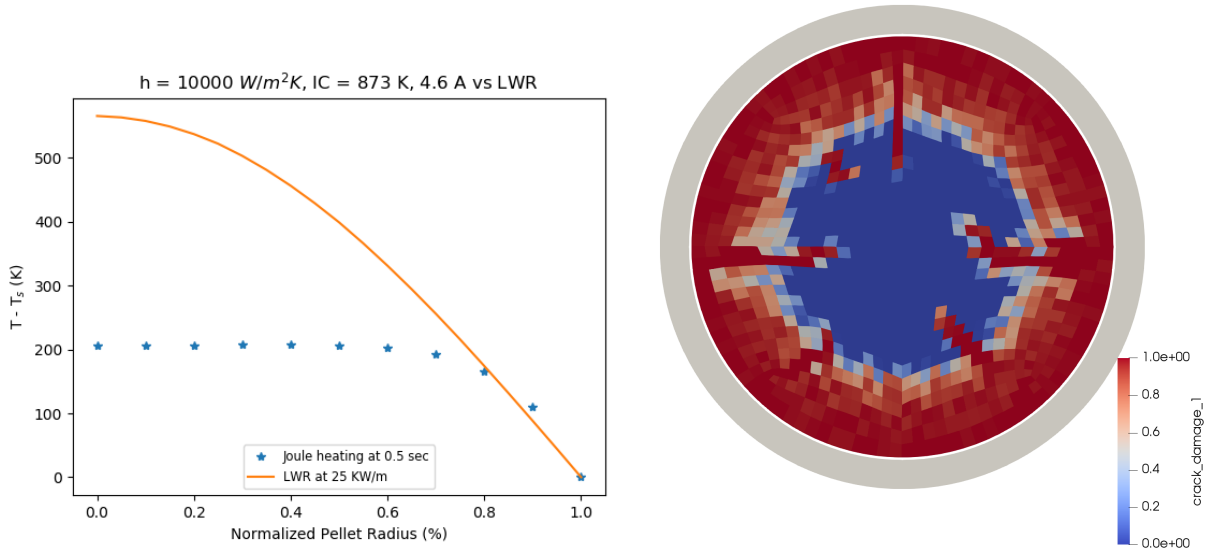

Figure 4-18: (a) Surface temperature gradient comparison with LWR. (b) Cracking of LWR at 25 KW/m.

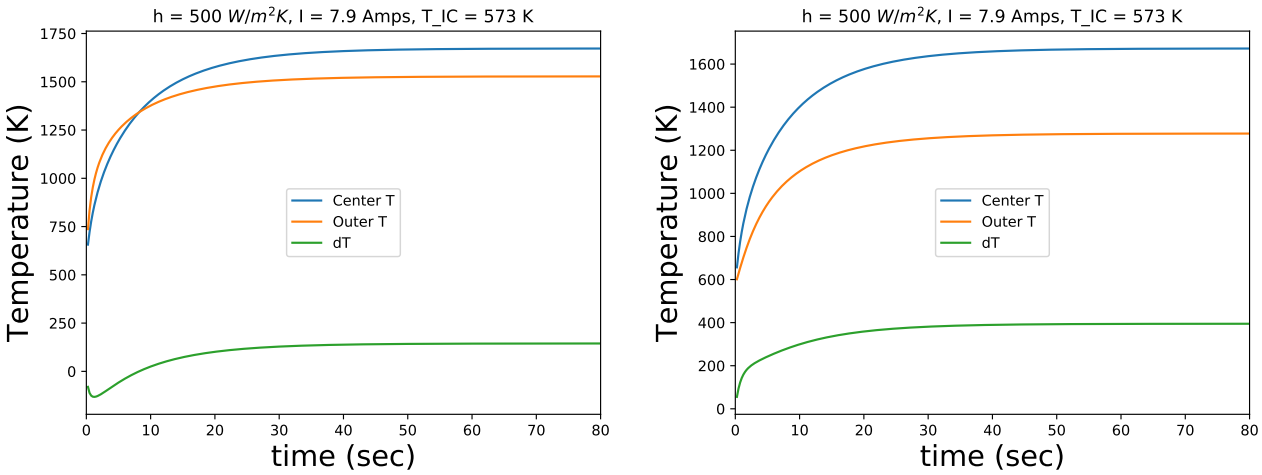

(a) On horizontal centerline.

(b) On vertical centerline.

Figure 4-19: Temperature time history

ture gradient on the horizontal centerline (Fig. 4-22).

4.4.3.2.2 Initial temperature = 673 K and current = 9.9 Amps

More cracks form (compared to the previous case) between electrodes (Fig. 4-23) and the equivalent power level is 23.8 KW/m (Fig. 4-24).

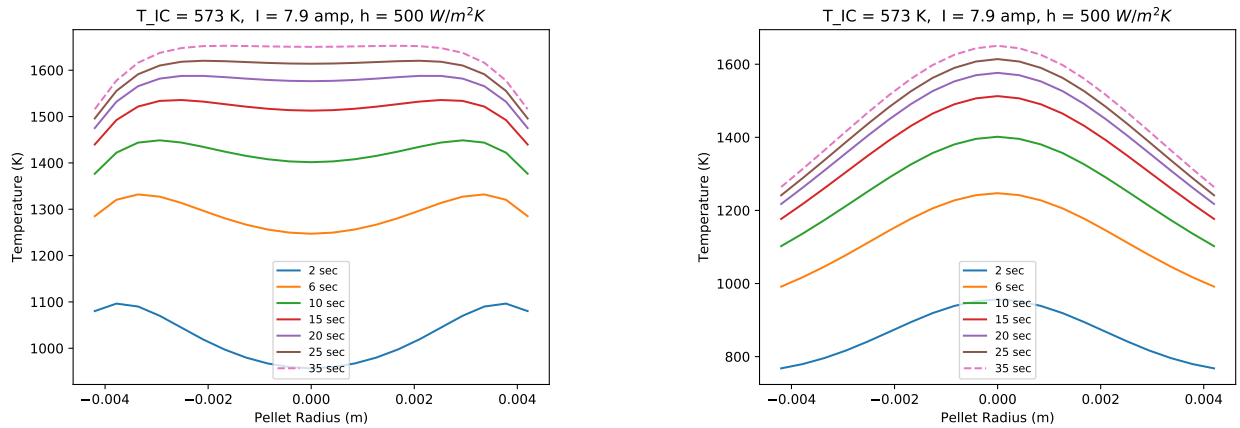

(a) On horizontal centerline.

(b) On vertical centerline.

Figure 4-20: Thermal results for simulation at constant current (7.9 amp) and initial pellet temperature 573 K.

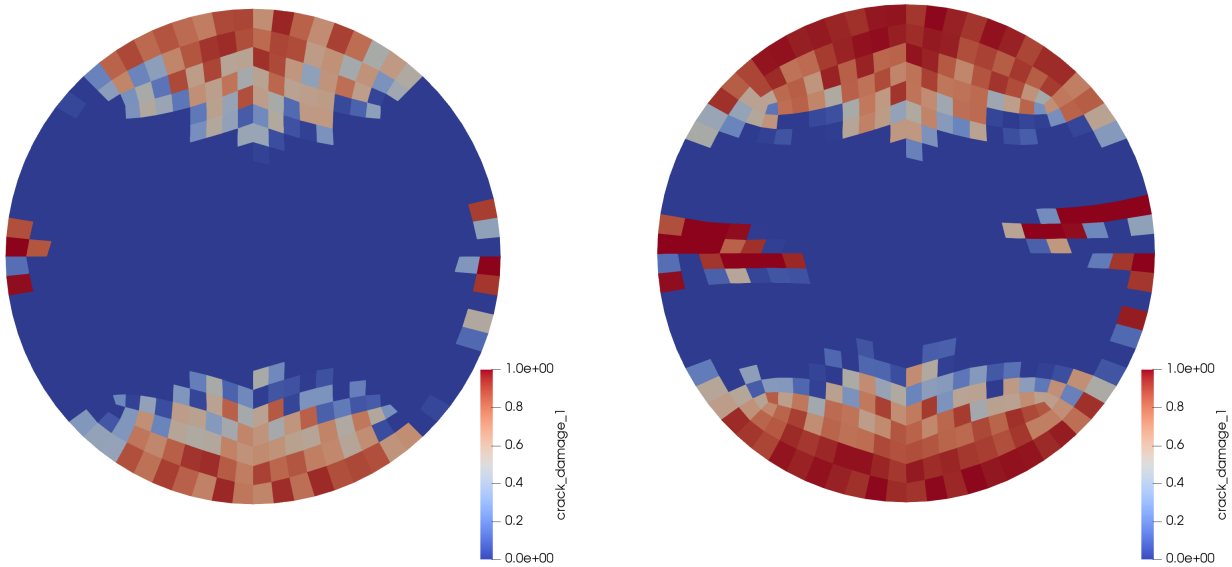

(a) Initial cracking at 1.5 seconds.

(b) Crack pattern at 12.25 seconds.

Figure 4-21: Crack patterns for h = 500 W/m^2K, T_{init} = 573 K and current = 7.9 Amps.

4.4.3.3 h = 10 W/m^2K

As the convective heat transfer coefficient is very low, the temperature distribution inside the pellet becomes flat (Fig. 4-25); that is the temperature reaches the average temperature faster than previous cases. Thus crack patterns are similar as the temperature gradient re-

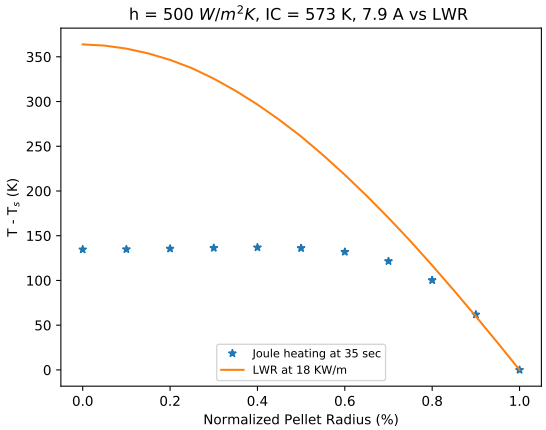

(a)

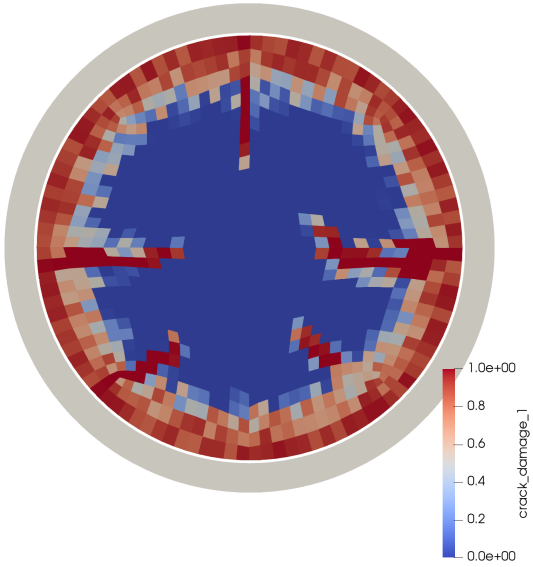

(b)

Figure 4-22: (a) Comparison of temperature gradient with LWR. (b) Cracking pattern of LWR at 18 KW/m power level.

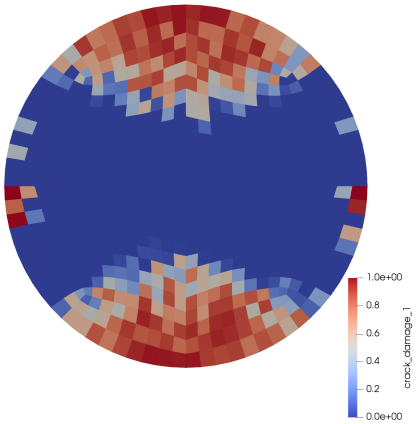

(a) Initial cracking at 1.5 seconds.

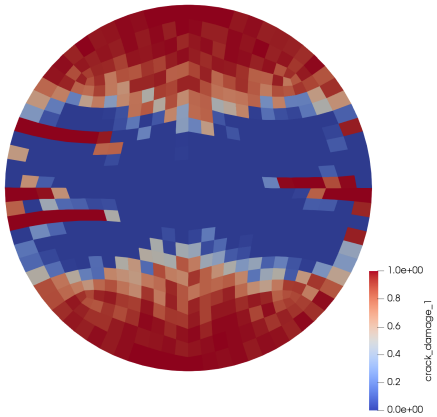

(b) Crack pattern at 12.5 seconds.

Figure 4-23: Crack patterns for h = 500 W/m^2K, T_{init} = 673 K and current = 9.9 Amps

duces on the vertical centerline and hardly any cracks form along the horizontal centerline (Fig. 4-26).

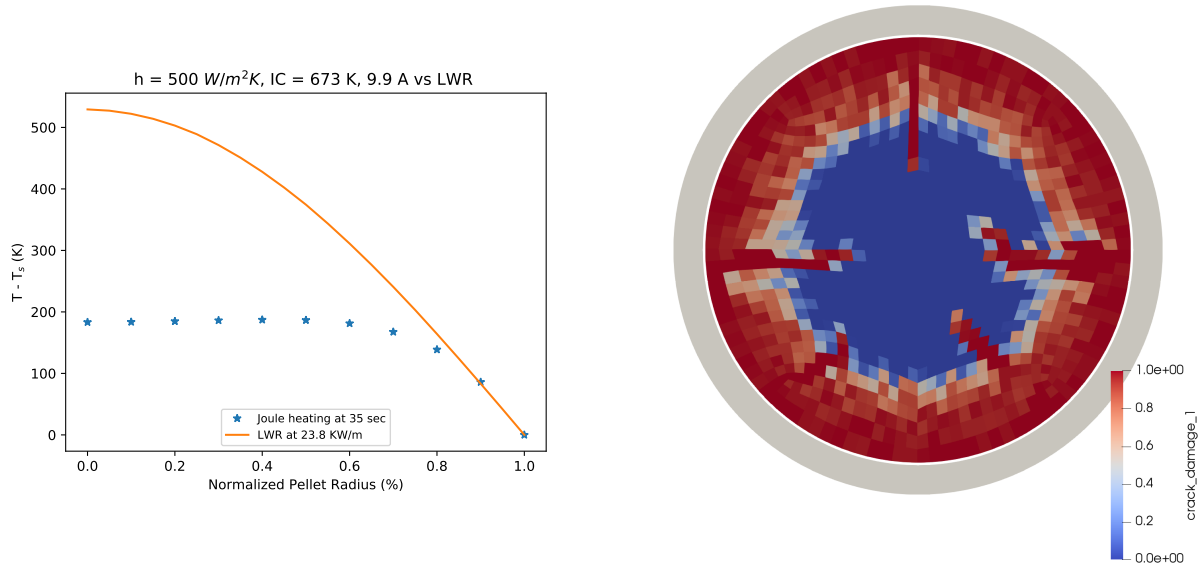

Figure 4-24: (a) Comparison of temperature gradient with LWR. (b) Cracking pattern of LWR at 23.8 KW/m power level.

4.4.4 Argonne DEH Experiment

In these experiments, paste was used between the pellets, and between the pellets and electrodes, to insure continuous electrical current along the vertical direction. Thus, one whole column of the seven pellets was setup in the simulation in an axisymmetrical system. Fig. 4-27 shows the cracking pattern, temperature distribution, current density and heat gener-

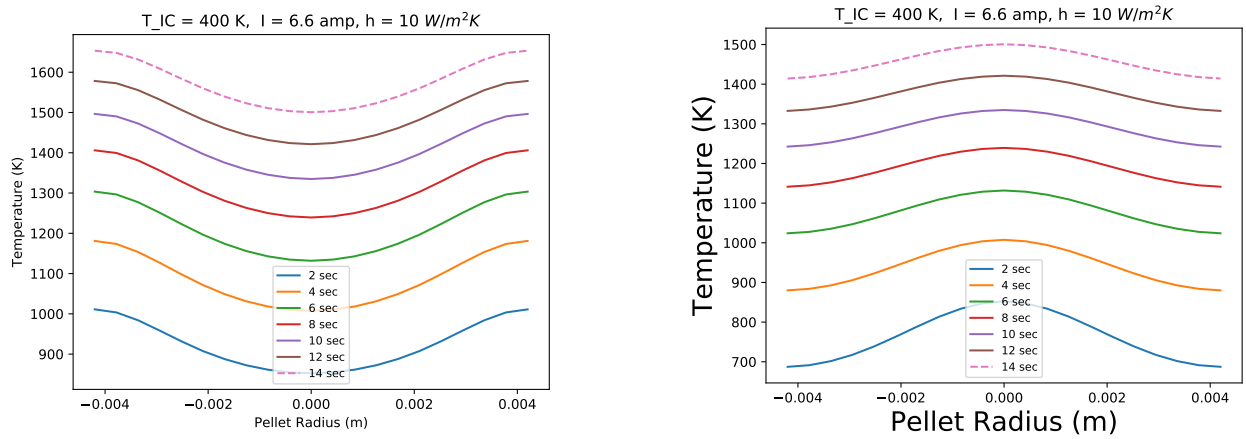

(a) On horizontal centerline.

(b) On vertical centerline.

Figure 4-25: Thermal results for simulation at constant current (6.6 amp) and initial pellet temperature 400 K.

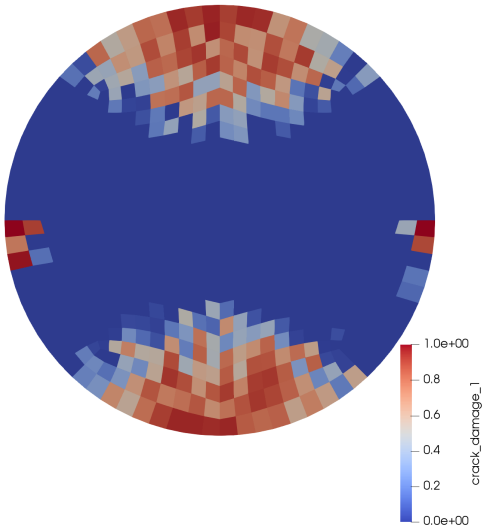

(a) Initial temperature = 400 K and current = 6.6 Amps

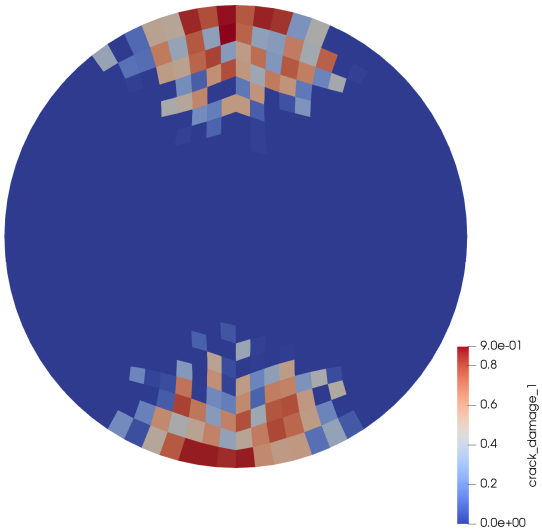

(b) Initial temperature = 573 K and current = 6.6 Amps

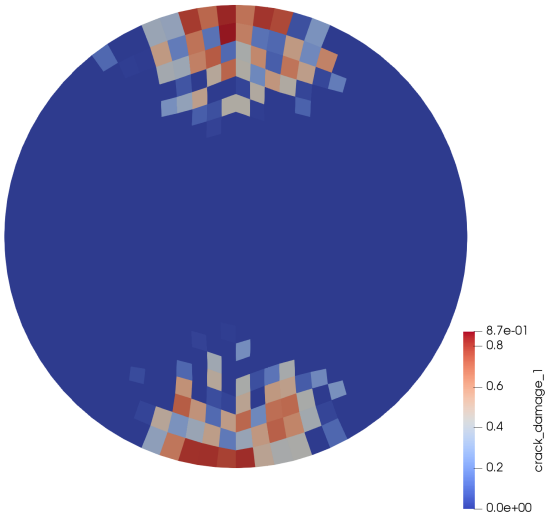

(c) Initial temperature = 673 K and current = 6.6 Amps

Figure 4-26: Cracking patterns at different initial temperatures

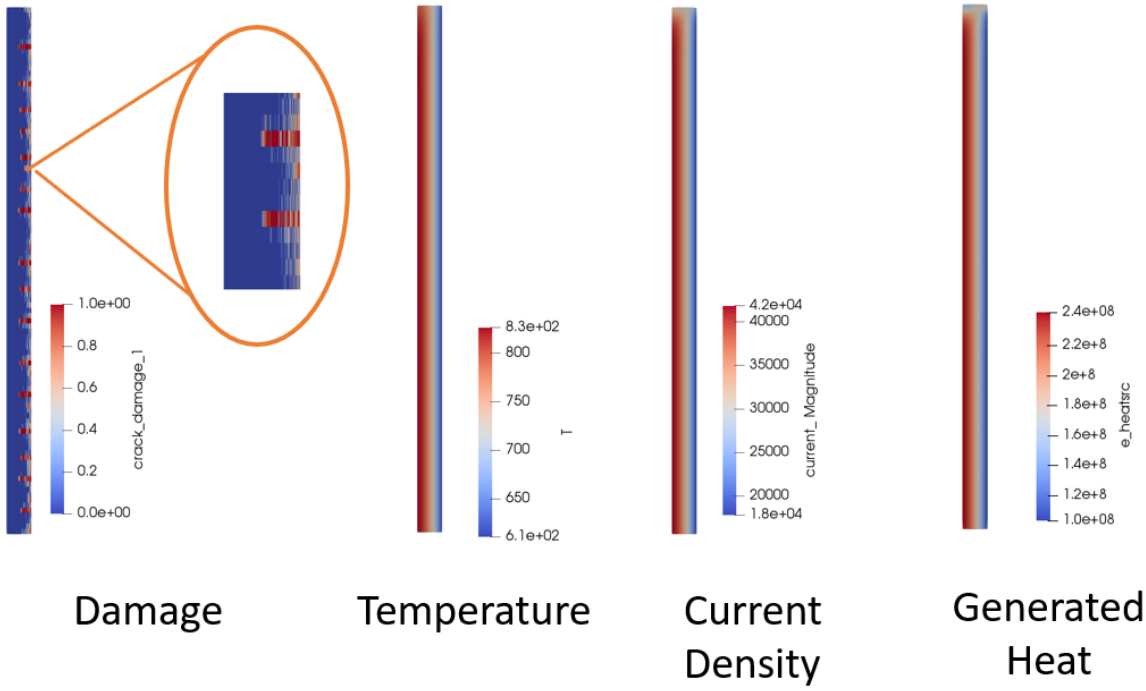

Figure 4-27: Simulation output for axisymmetric DEH experiment

ated in the pellets. However, these experiments were designed for empirical modeling and there was not enough data to benchmark the simulation codes.

Chapter 5

Summary

The objective of this project is to guide experiment designs that will create the temperature gradient near the pellet surface that is needed to induce cracking. Simulation results provide the parameter range that would produce valuable data for validation.

Bison models have been established to simulate LWR slow ramping rise to power in 1-D and 2D cylindrical coordinates; thermal/mechanical models were developed for UO_2 thermal shock experiments and electrical/thermal/mechanical models were developed for Joule heating experiments. Equivalent power levels in LWR can be determined by comparing temperature profile or temperature gradients near pellet surfaces with experiment simulation results. By adjusting parameters, similar thermal stress induced crack propagation can be found in both out-of-pile experiments to those found in LWR's.

5.1 Thermal Shock

Experiment concept is to quench hot pellet in cold bath to obtain the high temperature gradient near the pellet surface. To achieve this, high gap conductance and high coolant heat transfer are preferred. Copper foil is chosen to improve heat conductance across the pellet cladding gap and as it is compressible it does not interfere with pellet thermal expansion and

cracking. However, it is not useful if the thermal conductivity is not reproducible because of inconsistent contact of copper foil layers. Yet, the results are similar to LWR conditions when the thermal conductivity in the gap is over 10 W/mK.

Heat transfer through the coolant was found to be a controlling factor in crack formation. Cracking starts at $h = 750W/m^2K$ and the cracking pattern is comparable to a 16 KW/m power level at $h = 3000W/m^2K$. The use of stainless steel (thermal conductivity $\approx$ 16 W/mk) or other materials with lower thermal conductivity as surrogate pellets to observe temperature difference between centerline and surface will likely improve model validation results over a broader range. If possible, regular ceramic rods can be examined to evaluate the cracking patterns to further relate effect of thermomechanical conditions on crack initiation and propagation. Also offset pellet position (instead of centered) in the assembly can be considered in the experiments. Heat transfer can be improved on the narrow gap side (or direct contact), thus, cracking can be observed at lower shock.

5.2 Joule Heating

The concept of this experiment design is to apply current to the pellet to generate heat as UO_2 is a semiconductor material.

A SemiconductorLinearConductivity module has been merged into the MOOSE framework, and it was demonstrated that this temperature dependent electrical conductivity model can be linked with the Joule heating heat source code and coupled with existing thermal/mechanical models. The full version of the Steinhart-Hart equation now can be extended easily to be used for overheating problems in the semiconductor sector.

DiffusionFluxAux, an AuxKernel was used to compute the components of the flux vec-

tor for diffusion problems and has also been merged into MOOSE.

JouleHeatingHeatSourceAux, an AuxKernel, is used to compute the heat generated from electrical resistance for Joule heating problems, and is ready to be merged into MOOSE.

Bibliography

S. Aronson, J. E. Rulli, and B. E. Schaner. Electrical properties of nonstoichiometric uranium dioxide. The Journal of Chemical Physics, 35(4):1382–1388, Oct 1961. doi: 10.1063/1.1732057.

S. Banerjee and T. R. Govindan Kutty. Functional Materials: Preparation, Processing & Applications, chapter 10 Nuclear Fuel, pages 387 – 466. 2012.

J. L. BATES, C. A. HINMAN, and T. KAWADA. Electrical conductivity of uranium dioxide. Journal of the American Ceramic Society, 50(12):652–656, dec 1967. doi: 10.1111/j.1151-2916.1967.tb15021.x.

Bison. `https://bison.inl.gov`, 2018.

T. England and B. Rider. Evaluation and compilation of fission product yields. Technical report, Los Alamos National Laboratory, 1994. Report LA-uR-94-3106, ENDF-349.

J.K. Fink. Thermophysical properties of uranium dioxide. Journal of Nuclear Materials, 279 (1):1–18, mar 2000. doi: 10.1016/s0022-3115(99)00273-1.

Philippe Garcia, Elisabetta Pizzi, Boris Dorado, David Andersson, Jean-Paul Crocombette, Chantal Martial, Guido Baldinozzi, David Siméone, Serge Maillard, and Guillaume Martin. A defect model for UO_{2+x} based on electrical conductivity and deviation from stoichiometry measurements. Journal of Nuclear Materials, 494:461–472, oct 2017. doi: 10.1016/j.jnucmat.2017.03.033.

Derek Gaston, Chris Newman, Glen Hansen, and Damien Lebrun-Grandié. MOOSE: A parallel computational framework for coupled systems of nonlinear equations. Nuclear Engineering and Design, 239(10):1768–1778, oct 2009. doi: 10.1016/j.nucengdes.2009.05.021.

Dávid Halabuk and Jiří Martinec. Calculation of stress and deformation in fuel rod cladding during pellet-cladding interaction. Acta Polytechnica, 55(6):384, dec 2015. doi: 10.14311/ap.2015.55.0384.

J. D. Hales, R. L. Williamson, S. R. Novascone, G. Pastore, B. W. Spencer, D. S. Staford, K. A. Gamble, D. M. Perez, and W. Liu. Bison theory manual, the equations behind nuclear fuel analysis. Technical Report BISON Release 1.2, Idaho National Laboratory, September 2015. INL/EXT-13-29930 Rev. 3.

J.D. Hales, R.L. Williamson, S.R. Novascone, D.M. Perez, B.W. Spencer, and G. Pastore. Multidimensional multiphysics simulation of TRISO particle fuel. Journal of Nuclear Materials, 443(1-3):531–543, nov 2013. doi: 10.1016/j.jnucmat.2013.07.070.

Frank P. Incropera and David P. DeWitt. Introduction to Heat Transfer. Wiley, 2011.

Tamotsu Ishii, Keiji Naito, and Keichi Oshima. Electrical conductivity and defect structures in non-stoichiometric uo2x. Journal of Nuclear Materials, 36(3):288–296, Sept 1970. doi: 10.1016/0022-3115(70)90044-9.

C. R. Kennedy, R. A. Christensen, and R. F. Eibert. UO2 pellet fragment relocation: kinetics and mechanics. Technical report, Argonne National Lab and Entropy Limited, 1979.

Arthur T. Motta and Donald R. Olander. Light Water Reactor Materials Volume 1: Fundamentals. American Nuclear Society, 2017. ISBN 9780894484612. URL https://www.amazon.com/Light-Water-Reactor-Materials-Fundamentals/dp/0894484613?SubscriptionId=0JYN1NVW651KCA56C102&tag=techkie-20&linkCode=xm2&camp=2025&creative=165953&creativeASIN=0894484613.

D. Olander. Nuclear fuels – present and future. Journal of Nuclear Materials, 389(1):1–22, may 2009. doi: 10.1016/j.jnucmat.2009.01.297. file:///C:/Users/Ju-Yuan

D.R. Olander. Light water reactor fuel design and performance. In Encyclopedia of Materials: Science and Technology, pages 4490–4504. Elsevier, 2001. doi: 10.1016/b0-08-043152-6/00787-7.

Charles Patterson and Friedrich Garzarolli. Processes going on in nonfailed rod during normal operation. Technical Report Vol I, Advanced Nuclear Technology International, September 2010.

Y.R. Rashid. Ultimate strength analysis of prestressed concrete pressure vessels. Nuclear Engineering and Design, 7(4):334–344, apr 1968. doi: 10.1016/0029-5493(68)90066-6. print.

E. C. Robertson, R. Raspet, J. H. Swartz, and M. E. Lillard. Properties of thermistors used in geothermal investigations. U. S. Geol. Surv. Bull., pages 1203–B, 1966. 33 pages.

A. M. Ross and R. L. Stoute. Heat transfer coefficient between uo2 and zircaloy-2. technical report aecl-1552. Technical report, Atomic Energy of Canada Limited, 1962.

Peter Rudling and Charles Patterson. Fuel material technology report volume iv. Technical report, Advanced Nuclear Technology International, February 2009.

Peter Rudling, Ron Adamson, Hubert Bairiot, Brian Cox, Peter Ford, Friedrich Garzarolli, Rolf Riess, and Alfred Strasser. Fuel material technology report volume ii. Technical report, Advanced Nuclear Technology International, 2007.

P. Ruello, G. Petot-Ervas, C. Petot, and L. Desgranges. Electrical conductivity and thermoelectric power of uranium dioxide. Journal of the American Ceramic Society, 88(3):604–611, mar 2005. doi: 10.1111/j.1551-2916.2005.00100.x. file:///C:/Users/Ju-Yuanprint.

B. Schultz. U : uranium. Supplement vol. C 5, Uranium dioxide, UO2, physical properties, electrochemical behavior, volume C5, handbook supplement Electrical and magnetic properties, pages 206–228. 1986 edition, 1986.

F.N. Skomurski, J.W. Wang, R.C. Ewing, and U. Becker. Charge distribution and oxygen diffusion in hyperstoichiometric uranium dioxide UO_{2+x} ($x \leqslant 0.25$). Journal of Nuclear Materials, 434(1-3):422–433, mar 2013. doi: 10.1016/j.jnucmat.2011.09.003.

John S. Steinhart and Stanley R. Hart. Calibration curves for thermistors. Deep Sea Research and Oceanographic Abstracts, 15(4):497–503, aug 1968. doi: 10.1016/0011-7471(68)90057-0.

H. Wang and R. N. Singh. Thermal shock behaviour of ceramics and ceramic composites. International Materials Reviews, 39(6):228–244, Jan 1994. doi: 10.1179/imr.1994.39.6.228.

James R. Welty, Charles E. Wicks, Robert E. Wilson, and Gregory L. Rorrer. Fundamentals of Momentum, Heat and Mass transfer. John Wiley and Sons, 2007.

R.L. Williamson, J.D. Hales, S.R. Novascone, M.R. Tonks, D.R. Gaston, C.J. Permann, D. Andrs, and R.C. Martineau. Multidimensional multiphysics simulation of nuclear fuel behavior. Journal of Nuclear Materials, 423(1-3):149–163, apr 2012. doi: 10.1016/j.jnucmat.2012.01.012.

S.J. Zinkle and G.S. Was. Materials challenges in nuclear energy. Acta Materialia, 61(3):735–758, feb 2013. doi: 10.1016/j.actamat.2012.11.004.